

# Nanoporous Materials

---

*Advanced Techniques for*  
**Characterization,  
Modeling,  
and Processing**

---

**Edited by Nick Kanellopoulos**



CRC Press  
Taylor & Francis Group

# **Nanoporous Materials**

---

*Advanced Techniques for*  
**Characterization,  
Modeling,  
and Processing**



# Nanoporous Materials

---

*Advanced Techniques for*  
**Characterization,  
Modeling,  
and Processing**

**Edited by Nick Kanellopoulos**



**CRC Press**

Taylor & Francis Group

Boca Raton London New York

---

CRC Press is an imprint of the  
Taylor & Francis Group, an **informa** business

CRC Press  
Taylor & Francis Group  
6000 Broken Sound Parkway NW, Suite 300  
Boca Raton, FL 33487-2742

© 2011 by Taylor and Francis Group, LLC  
CRC Press is an imprint of Taylor & Francis Group, an Informa business

No claim to original U.S. Government works

Printed in the United States of America on acid-free paper  
10 9 8 7 6 5 4 3 2 1

International Standard Book Number-13: 978-1-4398-1105-4 (Ebook-PDF)

This book contains information obtained from authentic and highly regarded sources. Reasonable efforts have been made to publish reliable data and information, but the author and publisher cannot assume responsibility for the validity of all materials or the consequences of their use. The authors and publishers have attempted to trace the copyright holders of all material reproduced in this publication and apologize to copyright holders if permission to publish in this form has not been obtained. If any copyright material has not been acknowledged please write and let us know so we may rectify in any future reprint.

Except as permitted under U.S. Copyright Law, no part of this book may be reprinted, reproduced, transmitted, or utilized in any form by any electronic, mechanical, or other means, now known or hereafter invented, including photocopying, microfilming, and recording, or in any information storage or retrieval system, without written permission from the publishers.

For permission to photocopy or use material electronically from this work, please access [www.copyright.com](http://www.copyright.com) (<http://www.copyright.com/>) or contact the Copyright Clearance Center, Inc. (CCC), 222 Rosewood Drive, Danvers, MA 01923, 978-750-8400. CCC is a not-for-profit organization that provides licenses and registration for a variety of users. For organizations that have been granted a photocopy license by the CCC, a separate system of payment has been arranged.

**Trademark Notice:** Product or corporate names may be trademarks or registered trademarks, and are used only for identification and explanation without intent to infringe.

**Visit the Taylor & Francis Web site at**  
**<http://www.taylorandfrancis.com>**

**and the CRC Press Web site at**  
**<http://www.crcpress.com>**

---

# Contents

---

|                   |     |
|-------------------|-----|
| Preface.....      | vii |
| Editor.....       | ix  |
| Contributors..... | xi  |

## Part I Basic Principles, Recent Advances, and Expected Developments of Advanced Characterization Techniques

|   |            |
|---|------------|
| <b>1 Scattering Techniques .....</b>  | <b>3</b>   |
| <i>Gérald Lelong, David L. Price, and Marie-Louise Saboungi</i>   |            |
| <b>2 Studying Diffusion and Mass Transfer at the Microscale.....</b>  | <b>53</b>  |
| <i>Christian Chmelik, Douglas M. Ruthven, and Jörg Kärger</i>   |            |
| <b>3 Nanoscale Microscopies .....</b>   | <b>95</b>  |
| <i>Anthony A.G. Tomlinson</i>   |            |
| <b>4 Calorimetric Techniques.....</b>   | <b>129</b> |
| <i>Philip L. Llewellyn</i>  |            |
| <b>5 Combination of In Situ and Ex Situ Techniques for Monitoring and Controlling the Evolution of Nanostructure of Nanoporous Materials.....</b> | <b>165</b> |
| <i>G.N. Karanikolos, F.K. Katsaros, G.E. Romanos, K.L. Stefanopoulos, and N.K. Kanellopoulos</i>  |            |

## Part II Fundamentals, Recent Advances, and Expected Developments of Simulation Methods

|  |            |
|--|------------|
| <b>6 Mesoscopic Methods.....</b>   | <b>223</b> |
| <i>P.M. Adler and J.-F. Thovert</i>  |            |
| <b>7 Characterization of Macroscopically Nonhomogeneous Porous Media through Transient Gas Sorption or Permeation Measurements .....</b> | <b>253</b> |
| <i>J.H. Petropoulos and K.G. Papadokostaki</i>   |            |

### **Part III Fundamentals, Recent Advances and Improvements, Membrane, Catalytic and Novel Processes Involving Nanoporous Materials**

- 8 Synthesis Processes of Nanoporous Solids**..... 283  
*P. Cool, V. Meynen, and E.F. Vansant*
- 9 Sorption Processes**..... 307  
*F. Rodríguez-Reinoso, A. Sepúlveda-Escribano, and J. Silvestre-Albero*
- 10 Fundamental Approach to Supercritical Hydrogen Adsorptivity of Nanoporous Carbons** ..... 353  
*Shigenori Utsumi and Katsumi Kaneko*
- 11 Membrane Processes**..... 387  
*A.F.P. Ferreira, M.C. Campo, A.M. Mendes, and F. Kapteijn*
- 12 Diffusional Transport in Functional Materials: Zeolite, MOF, and Perovskite Gas Separation Membranes, Proton Exchange Membrane Fuel Cells, Dye-Sensitized Solar Cells** ..... 423  
*J. Caro*
- 13 Zeolites and Mesoporous Aluminosilicates as Solid Acid Catalysts: Fundamentals and Future Challenges** ..... 449  
*Ana Primo, Avelino Corma, and Hermenegildo García*

### **Part IV Case Studies of Applications of Advanced Techniques in Involving Nanoporous Materials**

- 14 Recent Developments in Gas-to-Liquid Conversion and Opportunities for Advanced Nanoporous Materials**..... 481  
*Gabriele Centi and Siglinda Perathoner*
- 15 Advanced Materials for Hydrogen Storage**..... 513  
*Th.A. Steriotis, G.C. Charalambopoulou, and A.K. Stubos*
- Index** ..... 549

---

## *Preface*

---

The advancement of materials science, nanotechnology, and biosciences depends on the effective use of advanced characterization and modeling techniques. During the last 30 years, there has been a tremendous improvement in the field of porous materials, with the development of increasing numbers of novel materials. During the same period, there have also been large numbers of significant breakthroughs in the development of advanced characterization and simulation techniques and their combinations. Since all the recent developments are largely scattered in a number of journals and conference proceedings, I believe that the concise information provided in this book covering diverse subjects will be a very useful reference for all scientists involved in the field of porous materials. This book aims to provide academic and industrial researchers of different disciplines and backgrounds with a concise yet comprehensive presentation of the state-of-the-art, recent developments, and expected improvements of advanced characterization and simulation techniques and their applications to optimize processes involving sorbents, membranes, and catalysts.

Nanoporous materials play an important role in chemical processing as, in many cases, they can successfully replace traditional, pollution-prone, and energy-consuming separation processes. These materials are widely used as sorbents, catalysts, catalyst supports, and membranes, and form the basis of innovative technologies, including high-temperature molecular sieve membrane separations and low-temperature reverse sorption membrane separations (hydrogen production, carbon dioxide capture and conversion, alkane/alkene separation, methane conversion, hydrogen storage, FCC catalysis, etc.). This is mainly due to their unique structural or surface physicochemical properties, which can, to an extent, be tailored to meet specific process-related requirements. Any equilibrium or dynamic process taking place within the nanopores of a solid is strongly influenced by the topology and the geometrical disorder of the pore matrix. The complete characterization of nanoporous materials still remains a difficult and frequently controversial problem, even if the equilibrium and transport mechanisms themselves are quite simple and well defined. This is mainly due to the great difficulty in accurately representing the complex morphology of the pore matrix. To this end, the application of combined techniques aided by advanced model analysis is of major importance as it is the most powerful method currently followed. On the other hand, no matter how thorough and complete the characterization, it is quite pointless if it is not related to the process under consideration, since one of the most important parameters in any application is the material's ability to retain its properties over a certain period of time. The "changes" induced on materials during their utilization in specific

applications are highly relevant and crucial for the economic viability of many applications (e.g., catalysis and separation processes). In this context, it is necessary to develop skills in establishing advanced combinations of “in situ” and “ex situ” techniques in order to expand our understanding of confinement phenomena in nanopores, to monitor and control the evolution of the properties of nanostructured materials, and to evaluate and optimize the performance of nanoporous sorbents, membranes, and catalysts involved in several important industrial processes.

The book is organized as follows: Part I presents the basic principles and major applications of the most important characterization techniques, ranging from diffraction and spectroscopy to calorimetry, permeability, and other techniques. Part II presents computer simulation techniques, an indispensable complement to the combination of the aforementioned analytical techniques. Part III covers the fundamentals and the recent advances in sorption, membrane, and catalyst processes, while Part IV presents two characteristic “case” studies of emerging areas of application of porous solids in the fields of gas-to-liquid conversion and hydrogen storage.

This book is based on the experience gained from the workshops organized by the network of excellence INSIDE-PORES and is mainly the result of the workshop on NAnoPorous Materials for ENvironmental and ENergy Applications (NAPEN 2008), which was organized in Crete by three cooperating European networks of excellence, namely, the Networks of Excellence IDECAT on catalysis, the NANOMEMBRO on membranes, and the INSIDE-PORES. I would like to thank Professors Gabriele Centi and Gilbert Rios, the coordinators of the cooperating networks of Excellence IDECAT and NANOMEMBRO. I would also thank my colleagues and students from Demokritos, A. Sapalides, G. Romanos, A. Labropoulos, S. Papageorgiou, V. Favvas, N. Kakizis, G. Pilatos, and E. Chatzidaki, for helping with the organization of NAPEN 2008. One of the major characteristics of this book is the impressive list of internationally well-known contributors. I would like to thank each one of them for their invaluable contributions. Special thanks are due to Jill Jurgensen and Allison Shatkin and their colleagues from Taylor & Francis Group for their help and patience. Last but not least, I would like to thank the European Commission for funding the three networks of excellence. I would also like to thank Dr. Soren Bowadt, who was in charge of these networks, for his valuable assistance and patience.

**Nick Kanellopoulos**

---

## *Editor*

---

**Nick Kanellopoulos** received his PhD from the Department of Chemical Engineering, University of Rochester, Rochester, New York, in 1975, and his diploma in chemical engineering from the National Technical University of Athens, Athens, Greece in 1970. He joined the Mass Transport Laboratory, Institute of Physical Chemistry, National Centre for Scientific Research Demokritos, Attiki, Greece, in 1976, and, since 1992, he has been the head of the “Membranes for Environmental Separations” Laboratory, NCSR Demokritos. His research interests include pore structure characterization, nanoporous membrane, and carbon nanotube systems, and the evaluation of their performance using a combination of in situ and ex situ techniques. Dr. Kanellopoulos is the author and coauthor of more than 140 papers; he is also the editor of *Recent Advances in Gas Separation by Microporous Membranes* (Elsevier Science) and the coeditor of *Nanoporous Materials for Energy and Environment* (Stanford Chong). He has received approximately 12 million euros in funding from over 50 European and national programs and has participated in three high technology companies in the field of nanoporous materials. He participated in the National Representation Committee of Greece for the FP6-NMP and FP7-NMP European programs in nanotechnology from 2001 to 2009. He is the coordinator of the European Network of Excellence in nanotechnology inside-pores.gr, a member of the Committee of the Kurchatov-Demokritos Project Center for Nanotechnology and Advanced Engineering, and the coordinator of the committee for the preparation and submission of the proposal for a Greek national nanotechnology program. He is also a Fulbright scholar and president of the Greek Fulbright Scholars Association.



---

# Contributors

---

**P.M. Adler**

Structure et Fonctionnement  
des Systèmes Hydriques  
Continentaux  
Université Pierre et Marie Curie  
Paris, France

**M.C. Campo**

Faculty of Engineering  
University of Porto  
Porto, Portugal

**J. Caro**

Institute of Physical Chemistry and  
Electrochemistry  
Leibniz University of Hannover  
Hannover, Germany

**Gabriele Centi**

Dipartimento di Chimica  
Industriale ed Ingegneria dei  
Materiali

and

Consorzio Interuniversitario  
Nazionale per la Scienza e  
Tecnologia dei Materiali  
Laboratorio di Catalisi per una  
Produzione Sostenibile e  
L'energia  
Università di Messina  
Messina, Italy

**G.C. Charalambopoulou**

Institute of Nuclear Technology  
and Radiation Protection  
National Center for Scientific  
Research "Demokritos"  
Athens, Greece

**Christian Chmelik**

Faculty of Physics and Geosciences  
University of Leipzig  
Leipzig, Germany

**P. Cool**

Laboratory of Adsorption and  
Catalysis  
Department of Chemistry  
University of Antwerpen  
Wilrijk, Belgium

**Avelino Corma**

Instituto Universitario de Tecnología  
Química  
Universidad Politécnica de  
Valencia  
Valencia, Spain

**A.F.P. Ferreira**

Faculty of Engineering  
University of Porto  
Porto, Portugal

**Hermenegildo García**

Instituto Universitario de Tecnología  
Química  
Universidad Politécnica de  
Valencia  
Valencia, Spain

**Katsumi Kaneko**

Department of Chemistry  
Graduate School of Science  
Chiba University  
Chiba, Japan

**N.K. Kanellopoulos**  
 Institute of Physical Chemistry  
 National Centre for Scientific  
 Research "Demokritos"  
 Athens, Greece

**F. Kapteijn**  
 Catalysis Engineering  
 Delft University of Technology  
 Delft, the Netherlands

**G.N. Karanikolos**  
 Institute of Physical Chemistry  
 National Centre for Scientific  
 Research "Demokritos"  
 Athens, Greece

**Jörg Kärger**  
 Faculty of Physics and Geosciences  
 University of Leipzig  
 Leipzig, Germany

**F.K. Katsaros**  
 Institute of Physical Chemistry  
 National Centre for Scientific  
 Research "Demokritos"  
 Athens, Greece

**Gérald Lelong**  
 Institute de Minéralogie et Physique  
 des Milieux Condensés  
 Université Paris 6

and

Centre National de la Recherche  
 Scientifique  
 Université Paris 7

and

Institut de Physique du Globe de  
 Paris  
 Institut de Recherche pour le  
 Développement  
 Paris, France

**Philip L. Llewellyn**  
 Laboratoire Chimie Provence  
 CNRS-Université de Provence  
 Marseille, France

**A.M. Mendes**  
 Faculty of Engineering  
 University of Porto  
 Porto, Portugal

**V. Meynen**  
 Laboratory of Adsorption and  
 Catalysis  
 Department of Chemistry  
 University of Antwerpen  
 Wilrijk, Belgium

**K.G. Papadokostaki**  
 Institute of Physical Chemistry  
 National Center for Scientific  
 Research "Demokritos"  
 Athens, Greece

**Siglinda Perathoner**  
 Dipartimento di Chimica  
 Industriale ed Ingegneria dei  
 Materiali

and

Consorzio Interuniversitario  
 Nazionale per la Scienza e  
 Tecnologia dei Materiali  
 Laboratorio di Catalisi per una  
 Produzione Sostenibile e  
 L'energia  
 Università di Messina  
 Messina, Italy

**J.H. Petropoulos**  
 Institute of Physical Chemistry  
 National Center for Scientific  
 Research "Demokritos"  
 Athens, Greece

**David L. Price**

Conditions Extrêmes et Matériaux:  
Haute Température et Irradiation  
Centre National de la Recherche  
Scientifique  
Université d'Orléans  
Orléans, France

**Ana Primo**

Instituto Universitario de Tecnología  
Química  
Universidad Politécnica de  
Valencia  
Valencia, Spain

**F. Rodríguez-Reinoso**

Laboratorio de Materiales  
Avanzados  
Departamento de Química  
Inorgánica  
Instituto Universitario de Materiales  
de Alicante  
Universidad de Alicante  
Alicante, Spain

**G.E. Romanos**

Institute of Physical Chemistry  
National Centre for Scientific  
Research "Demokritos"  
Athens, Greece

**Douglas M. Ruthven**

Department of Chemical  
Engineering  
University of Maine  
Orono, Maine

**Marie-Louise Saboungi**

Centre de Recherche sur la Matière  
Divisée  
Centre National de la Recherche  
Scientifique  
Université d'Orléans  
Orléans, France

**A. Sepúlveda-Escribano**

Laboratorio de Materiales  
Avanzados  
Departamento de Química  
Inorgánica  
Instituto Universitario de Materiales  
de Alicante  
Universidad de Alicante  
Alicante, Spain

**J. Silvestre-Albero**

Laboratorio de Materiales  
Avanzados  
Departamento de Química  
Inorgánica  
Instituto Universitario de Materiales  
de Alicante  
Universidad de Alicante  
Alicante, Spain

**K.L. Stefanopoulos**

Institute of Physical Chemistry  
National Centre for Scientific  
Research "Demokritos"  
Athens, Greece

**Th.A. Steriotis**

Institute of Physical Chemistry  
National Center for Scientific  
Research "Demokritos"  
Athens, Greece

**A.K. Stubos**

Institute of Nuclear Technology  
and Radiation Protection  
National Center for Scientific  
Research "Demokritos"  
Athens, Greece

**J.-F. Thovert**

Institut PPRIME SP2MI  
Futuroscope, France

**Anthony A.G. Tomlinson**

Consiglio Nazionale delle Ricerche  
Istituto per lo Studio dei Materiali  
Nanostrutturati  
Rome, Italy

**Shigenori Utsumi**

Department of Mechanical Systems  
Engineering  
Tokyo University of Science  
Chino, Japan

**E.F. Vansant**

Laboratory of Adsorption and  
Catalysis  
Department of Chemistry  
University of Antwerpen  
Wilrijk, Belgium

## **Part I**

# **Basic Principles, Recent Advances, and Expected Developments of Advanced Characterization Techniques**



# 1

---

## *Scattering Techniques*

---

Gérald Lelong, David L. Price, and Marie-Louise Saboungi

### CONTENTS

|          |   |    |
|----------|---|----|
| 1.1      | Introduction.....                                       | 4  |
| 1.2      | Diffraction.....  | 5  |
| 1.2.1    | Diffraction Formalism.....                              | 6  |
| 1.2.2    | Differences between Neutron and X-Ray Scattering.....   | 13 |
| 1.2.3    | Selected Example .....                                  | 14 |
| 1.3      | Small-Angle Scattering .....                            | 17 |
| 1.3.1    | SAS Spectrometer.....                                   | 17 |
| 1.3.2    | Small Angle Scattering vs. Diffraction .....            | 19 |
| 1.3.3    | What Does Q Probe?.....                                 | 19 |
| 1.3.4    | Small-Angle Scattering Formalism .....                  | 20 |
| 1.3.5    | SAS from a Two-Phase System.....                        | 21 |
| 1.3.5.1  | Guinier Approximation: Radius of Gyration.....          | 24 |
| 1.3.5.2  | Porod Scattering.....                                   | 25 |
| 1.3.5.3  | Porod Invariant.....                                    | 25 |
| 1.3.6    | Form Factors .....                                      | 26 |
| 1.3.7    | Multicomponent Systems: Neutron Contrast Matching ..... | 28 |
| 1.3.8    | Interacting Scatterers: Structure Factor .....          | 30 |
| 1.3.9    | SANS vs. SAXS.....                                      | 33 |
| 1.3.10   | Selected Examples.....                                  | 33 |
| 1.3.10.1 | Porous Materials.....                                   | 33 |
| 1.3.10.2 | Soft Matter.....  | 35 |
| 1.3.10.3 | New Developments.....                                   | 36 |
| 1.4      | X-Ray Absorption Spectroscopy .....                     | 37 |
| 1.5      | Inelastic Scattering.....                               | 38 |
| 1.5.1    | Selected Examples.....                                  | 44 |
|          | References.....   | 48 |

---

## 1.1 Introduction

Neutrons produced by reactors and spallation sources, and x-rays produced by synchrotron sources, have wavelengths in the range of 0.1–1 nm, making the scattering experiments a powerful and versatile probe of nanoporous materials. In fact it is hard to find a comprehensive paper on some aspect of confinement on the nm scale that does not include references to scattering measurements. A case in point is the excellent topical review of Alcoutlabi and McKenna<sup>1</sup> dealing with the effects of size and confinement on the melting temperature  $T_m$  (always depressed) and the glass transition temperature  $T_g$  (may increase, decrease, remain the same, or even disappear). Among other scattering results they refer to the work of Morineau et al.,<sup>2</sup> who measured the density of confined liquid toluene through changes in the Bragg peak intensity in neutron diffraction measurements resulting from the change in contrast with the confined liquid. Whereas little or no changes were observed for confinement in mesoporous silicates with pore sizes of 3.5 nm and above, a decrease in density and an *increase* of 30 K in  $T_g$  were observed upon confinement in 2.4 nm pores. Alcoutlabi and McKenna also refer to the inelastic neutron scattering (INS) studies of Zorn et al.<sup>3</sup> who observed a *decrease* in  $T_g$  on the confinement of salol in microporous silica glass together with a broadening of the relaxation spectra. These effects were discussed in terms of a cooperativity length scale that, since it cannot become larger than the confining dimensions, leads to an acceleration of the molecular dynamics compared with the bulk.

In this chapter, we summarize the techniques of diffraction—essentially, the study of correlations in atomic arrangements on the scale of 0.1–1 nm, sometimes referred to as wide-angle neutron or x-ray scattering (WANS, WAXS), small-angle scattering (SAS) that measures density fluctuations on the length scale of 5–500 nm, and inelastic scattering that probes dynamical phenomena on the timescale of 0.1 ps to 0.1 ms. We include a brief description of x-ray absorption spectroscopy, often used in conjunction with scattering experiments: for example, extended x-ray absorption fine-structure spectroscopy (EXAFS) provides an element-specific structural probe through the scattering of the emitted photoelectron by neighboring atoms. Figure 1.1 compares the length and timescales probed by different scattering techniques with optical, dielectric, and nuclear magnetic resonance (NMR) spectroscopies.

To flesh out these bare bones, we provide some examples of the application of these techniques from our own work, including selenium absorbed in zeolites, mesoporous silica nanopores, hydrogen adsorbed on carbon nanohorns, and glucose solutions confined in aqueous silica gels.

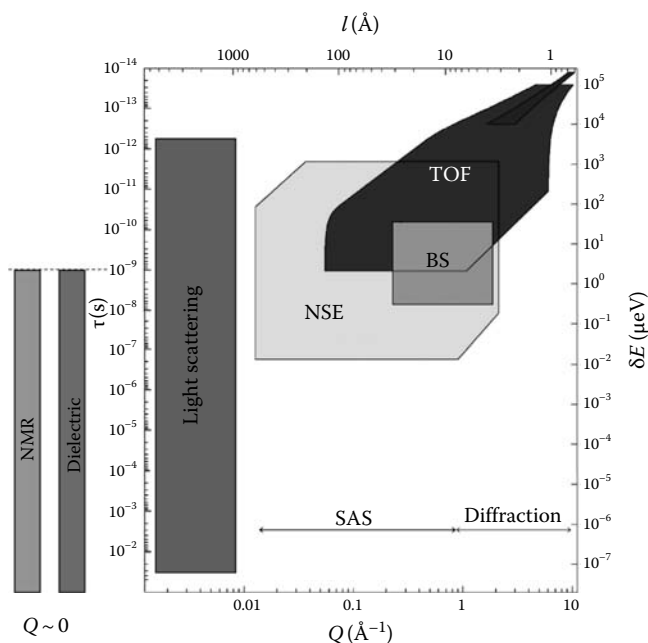


**FIGURE 1.1**

Schematic representation of accessible length and time scales using light or neutron scattering techniques (time-of-flight (ToF), backscattering (BS), neutron spin echo (NSE), and SAS spectrometers) and spectroscopic methods (nuclear magnetic resonance [NMR] and dielectric spectroscopy).

## 1.2 Diffraction

Diffraction is generally taken to mean the measurement of atomic or magnetic structure by scattering experiments. In principle, any particle can be used, but for most investigations of atomic structure neutrons, x-rays, and electrons are most common while neutrons and, in certain cases, x-rays can be also used to provide information about magnetic structure.

*The neutron* is a subatomic particle with, as its name implies, zero charge, mass  $m_n = 1.0087$  atomic mass units, spin  $I = \frac{1}{2}$  and magnetic moment  $\mu_n = -1.9132$  nuclear magnetons. These properties combine to make the neutron a highly effective probe of condensed matter. The zero charge means that its interactions with a sample of a condensed material are confined to the short-ranged nuclear and normally weak magnetic interactions, so that the neutron can usually penetrate into the bulk of the sample.

Thermal neutrons for condensed matter research are usually obtained by slowing down energetic neutrons, produced by a nuclear reaction in either a fission reactor or an accelerator-driven spallation source, by means of inelastic collisions in a moderating material consisting of light atoms. Most of the slow neutrons thus produced will have kinetic energies on the order of  $k_B T$  where  $T$  is the moderator temperature. Considering the wave nature of the neutron, its wavelength is given by

$$\frac{\hbar^2}{2m_n \lambda^2} = k_B T. \quad (1.1)$$

The neutron mass is such that for  $T=300\text{K}$ ,  $\lambda \sim 2\text{Å}$ , a distance comparable to the mean atomic separation in a solid or liquid. Such neutrons are therefore ideally suited to studies of the *atomic structure* of condensed matter, discussed below. Furthermore, the kinetic energy of such a neutron is on the order of  $25\text{meV}$ , a typical energy for excitations in solids and liquids. Thus, both wavelength and energy are ideally suited to studies of the *atomic dynamics* of condensed matter in inelastic scattering experiments, discussed in Section 1.5.

The magnetic moment of the neutron makes it a unique probe of *magnetic structure and excitations*: neutrons are scattered from the magnetic moments associated with unpaired electron spins in magnetic materials. Again, the wavelength and energy of a thermal neutron are such that both the magnetic structure and the dynamics of the spin system can be studied in the neutron scattering experiment.

The *x-ray* is a photon with an energy conventionally taken in the range of keV. It has zero charge, zero magnetic moment, and spin  $I=1$ . An x-ray of energy  $E=hc/\lambda=12.398\text{keV}$  has wavelength  $\lambda=1\text{Å}$ , making it also, as is well known, a powerful probe of the structure of condensed matter. The electromagnetic field associated with a moving x-ray makes it, under appropriate circumstances, another probe of magnetic structure. To probe excitations in condensed matter, which typically have energies in the meV range, an energy resolution on the order of  $10^{-7}$  is required in both incident and scattered beams, a formidable challenge that has recently been met in third-generation synchrotron sources.

### 1.2.1 Diffraction Formalism

We consider a simple scattering experiment shown schematically in Figure 1.2. We suppose that a beam of particles (neutrons, x-rays, or electrons) characterized by a wave vector  $\vec{k}_i$  falls on the sample. The magnitude of  $\vec{k}_i$  is  $2\pi/\lambda$  and its direction corresponds to that of the beam. Usually the sample size is chosen such that most of the beam is transmitted: typically it is  $\sim\text{mm}$  with neutrons, and with x-rays it varies from  $\sim\text{mm}$  for light atoms

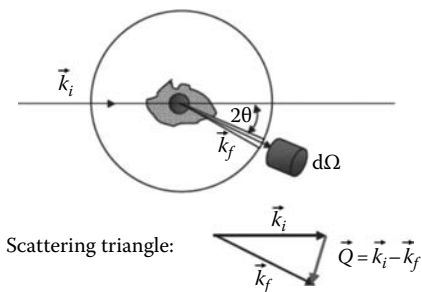


**FIGURE 1.2**  
Geometry of a typical diffraction experiment.

to  $\sim \mu\text{m}$  for heavy atoms. Some particles are, however, scattered and can be measured with a detector placed, for example, in a direction  $\vec{k}_f$ . If the incident beam is characterized by a flux  $\Phi$  (particles crossing unit area per unit time), the sample has  $N$  identical atoms in the beam, and the detector subtends solid angle  $\Delta\Omega$  and has efficiency  $\eta$ , we may expect the count rate in the detector to be proportional (if  $\Delta\Omega$  is small enough) to all these quantities. In this case, the constant of proportionality is called the differential cross section and is derived as<sup>4</sup>

$$\frac{d\sigma}{d\Omega} = \frac{C}{\eta\Phi N(\Delta\Omega)}. \quad (1.2)$$

The structural information obtained in a diffraction experiment is normally described by the variation of the intensity of the scattering with the scattering vector  $\vec{Q}$ :

$$\vec{Q} = \vec{k}_i - \vec{k}_f \quad (1.3)$$

illustrated by the triangle in Figure 1.2. In the case of experiments on samples that are directionally isotropic—polycrystalline solids, glasses, and liquids—the scattering depends only on the magnitude of the scattering vector, the scalar quantity  $Q = \|\vec{Q}\|$ .

It is usual to fix the directions of  $\vec{k}_i$  and  $\vec{k}_f$  by means of appropriate collimators, detector placement, etc. and to fix the magnitude of one of these, generally  $k_i$ , or sometimes a combination of  $k_i$  and  $k_f$ , for example one that corresponds to the total time-of-flight from sample to detector in the case of neutron scattering. The total intensity of the scattered particles measured in the detector is normally recorded, irrespective of any energy transfer that may take place, and  $\vec{Q}$  is evaluated from Equation 1.3 under the assumption that the scattering is elastic, i.e., there is no energy exchange between the particle and the sample and so  $|\vec{k}_i| = |\vec{k}_f|$ . In the neutron case, significant

inelastic scattering is always present and this can affect the structural interpretation. However, the experiments are usually designed to minimize the errors that result from these approximations, which can usually be taken care of by straightforward corrections. For elastic scattering,  $Q$  depends only on  $k_i$  and the scattering angle  $2\theta$ , corresponding to the Bragg relation  $Q = 4\pi \sin \theta / \lambda$ .

The nuclear interaction between a slow neutron and an atom can be expressed in a simple form. In the simplest case where the atoms in the sample are both noninteracting and identical, the differential cross section is just a constant:

$$\frac{d\sigma}{d\Omega} = b^2, \quad (1.4)$$

where the scattering length  $b$  is normally a constant, depending on the atomic number  $Z$  and the atomic weight  $A$  of the nucleus, and its spin state relative to that of the neutron. Its magnitude depends on the details of the interaction between the neutron and the components of the nucleus. For this reason both sign and magnitude of  $b$  change in an irregular fashion with  $Z$  and  $A$ .

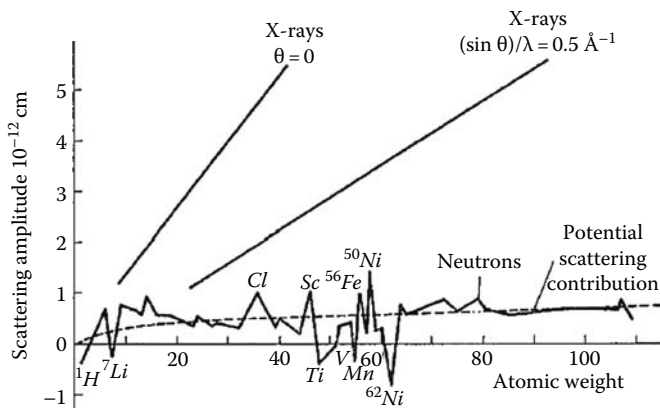
In the x-ray case, the photon interacts with the electrons in the atom, and since these are distributed in space, the scattering factor is proportional to the total number of electrons and a form factor that represents the Fourier transform of their radial distribution. The differential cross section is then a function of the scattering vector  $Q$ :

$$\frac{d\sigma}{d\Omega} = f^2(Q). \quad (1.5)$$

In contrast with the neutron case, the x-ray scattering, which increases monotonically with  $Z$ , is independent of isotope and decreases with  $Q$ . The scattering length for neutrons and scattering factor for x-rays for two values of  $\theta$ , and hence of  $Q$ , are shown in Figure 1.3.

For convenience, comparison between experiment and theory is usually done in terms of a dimensionless quantity, the *structure factor*  $S(Q)$ . In the case of neutron diffraction, this is related to the differential cross section by the relation:

$$\frac{d\sigma}{d\Omega} = \left| \sum_{a=1}^n c_a \bar{b}_a \right|^2 (S(Q) - 1) + \sum_{a=1}^n c_a \bar{b}_a^2, \quad (1.6)$$


**FIGURE 1.3**

Scattering lengths for neutrons and scattering factor for x-rays for two values of scattering angle  $2\theta$ , as a function of atomic weight  $A$ .

where

$c_a$  is the atomic concentration

$\bar{b}_a$  is the average (over isotopes and spin states) of the neutron–nucleus scattering length

$\bar{b}_a^2$  is the mean square scattering length of element  $a$  present in the sample.

This can be rewritten as follows:

$$\frac{d\sigma}{d\Omega} = \left| \sum_{a=1}^n c_a \bar{b}_a \right|^2 S(Q) + \left[ \sum_{a=1}^n c_a |\bar{b}_a|^2 - \left| \sum_{a=1}^n c_a \bar{b}_a \right|^2 \right] + \left[ \sum_{a=1}^n c_a (\bar{b}_a^2 - |\bar{b}_a|^2) \right], \quad (1.7)$$

where the leading term contains the structural information that is being sought here. The second term arises from random distributions of different elements (often referred to as *Laue diffuse scattering*) and the third term from random distributions of isotopes and spin states over the atoms belonging to a given element (generally called *incoherent scattering*). It is convenient to define the coherent and incoherent cross sections of element  $a$ :

$$\sigma_a^{\text{coh}} = 4\pi(\bar{b}_a)^2 \quad \text{and} \quad \sigma_a^{\text{inc}} = 4\pi[\bar{b}_a^2 - (\bar{b}_a)^2]. \quad (1.8)$$

It can be seen that the coherent cross sections enter into the first two terms of Equation 1.7 and the incoherent into the third. In the x-ray case, every atom of a given element scatters identically so the incoherent term does

**TABLE 1.1**

Neutron Scattering Lengths  $b$  in Femtometers (1 fm =  $10^{-15}$  m) and the Respective Coherent  $\sigma_{\text{coh}}$  and Incoherent  $\sigma_{\text{inc}}$  Scattering Cross Sections in Barns (1 barn =  $10^{-24}$  cm<sup>2</sup>) for Some Elements of the Periodic Table

| Element          | $b$ (fm) | $\sigma^{\text{coh}}$ (Barn) | $\sigma^{\text{inc}}$ (Barn) |
|------------------|----------|------------------------------|------------------------------|
| <sup>1</sup> H   | -3.742   | 1.758                        | 80.276                       |
| <sup>2</sup> H   | 6.674    | 5.593                        | 2.053                        |
| <sup>6</sup> Li  | 2.000    | 0.515                        | 0.465                        |
| <sup>7</sup> Li  | -2.222   | 0.619                        | 0.783                        |
| <sup>12</sup> C  | 6.653    | 5.559                        | 0                            |
| <sup>14</sup> N  | 9.372    | 11.035                       | 0.501                        |
| <sup>16</sup> O  | 5.805    | 4.232                        | 0                            |
| <sup>19</sup> F  | 5.654    | 4.017                        | 0.001                        |
| <sup>23</sup> Na | 3.632    | 1.662                        | 1.623                        |
| <sup>27</sup> Al | 3.449    | 1.495                        | 0.008                        |
| <sup>28</sup> Si | 4.106    | 2.120                        | 0                            |
| <sup>31</sup> P  | 5.131    | 3.307                        | 0.005                        |
| <sup>32</sup> S  | 2.804    | 0.988                        | 0                            |
| <sup>70</sup> Ge | 10.010   | 12.63                        | 0                            |

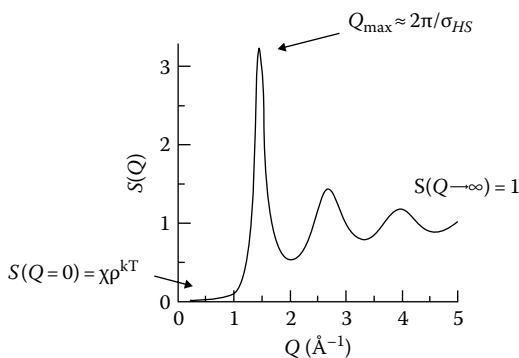
Source: Price, D.L. and Sköld, K., Introduction to neutron scattering, in *Neutron Scattering, Methods of Experimental Physics*, eds. D.L. Price and K. Sköld, Vol. 23 (Part A), p. 1, Academic Press, New York, 1986.

not appear. Table 1.1 gives the values of the neutron scattering lengths and the coherent and incoherent cross sections for a selection of elements and isotopes.

By definition,  $S(Q)$  tends to unity at large  $Q$ , a property that is often used to normalize the intensities measured in a diffraction experiment. Its low- $Q$  limit is related to the macroscopic compressibility  $\chi_T$ :

$$S(0) = \frac{\rho_0}{V} \left( \frac{\partial V}{\partial P} \right)_T k_B T = \rho_0 \chi_T k_B T, \quad (1.9)$$

where  $\rho_0$  is the number of atoms per unit volume. In between  $S(Q)$  exhibits a complex behavior that reflects the detailed atomic structure. In a crystalline sample—either single crystal or polycrystalline—there are sharp peaks called *Bragg peaks* that arise from diffraction from parallel crystallographic planes at  $Q$  values corresponding to  $2\pi n/d$ , where  $n$  is an integer and  $d$  the plane spacing. There is also a continuous component, called *diffuse scattering*, arising from static and/or dynamic disorder. In

**FIGURE 1.4**

Typical form for  $S(Q)$  in a simple classical liquid or glass. (From Price, D.L., *Experimental techniques, in High-Temperature Levitated Materials*, Cambridge University Press, Cambridge, U.K., p. 45, 2010. With permission.)

fully disordered materials like liquids and glasses, the entire scattering is diffuse, with a generally oscillatory pattern that reflects the short- and intermediate-range order in the sample. A well-defined distance of closest approach between atoms that can be characterized by an equivalent hard-sphere diameter  $\sigma_{HS}$  will be reflected in oscillations in  $S(Q)$  with a period  $2\pi/\sigma_{HS}$ . A typical form for  $S(Q)$  in a simple classical liquid is shown in Figure 1.4.

In the case of x-ray diffraction,  $b_a$  in the above equations and those that follow is replaced by  $f_a(Q)$ , the atomic form factor for species  $a$ . This results from the fact that the electrons in the atom from which the x-rays are scattered have a spatial distribution, while the nucleus from which the neutrons are scattered can be treated, for the present purposes, as a point object. Since the form factors are generally well tabulated this is not a major problem, but it can complicate the interpretation of the scattering from multicomponent systems.

A *pair correlation function*  $g(r)$  that contains the structural information about the sample in real space is then calculated from  $S(Q)$  *via* the Fourier transform

$$g(r) = 1 + \frac{1}{2\pi^2\rho_0} \int_0^{Q_{\max}} Q(S(Q) - 1) \frac{\sin Qr}{r} M(Q) dQ, \quad (1.10)$$

where  $M(Q)$  is a modification function that is often used to force the integrand to go smoothly to zero at  $Q_{\max}$  and reduce the ripples that result from the finite limit of the integration.

For systems with more than one type of atom—different elements, and sometimes different isotopes of the same element— $S(Q)$  is a weighted sum of partial structure factors  $S_{ab}(Q)$ . Unfortunately, there are a number of alternative definitions of these in the literature: the  $S(Q)$  appearing in Equations 1.6 through 1.9 is called the Faber–Ziman definition after

its originators.<sup>5</sup> Another definition of partial structure factors for binary systems was proposed by Bhatia and Thornton,<sup>6</sup> where  $S_{NN}(Q)$  describes the fluctuations in total particle density,  $S_{CC}(Q)$  those in the relative concentrations, and  $S_{NC}(Q)$  the cross-correlation of the two. For a two-component system Equation 1.9 applies to  $S_{NN}(Q)$ . The various definitions are linear combinations of each other and are given in the textbooks, for example, that of March and Tosi.<sup>7</sup>

For a multicomponent system,  $g(r)$  is correspondingly a weighted sum of partial pair correlation functions  $g_{ab}(r)$ , which in the neutron case is given by

$$g(r) = \sum_{a,b} W_{ab} g_{ab}(r) = \sum_{a,b} \frac{c_a c_b b_a b_b}{\left[ \sum_{a,b} c_a b_a \right]^2} g_{ab}(r), \quad (1.11)$$

where

$a$  and  $b$  are the atom types

$W_{ab}$  are weighting factors

The partial pair distribution function  $g_{ab}(r)$  can be considered as the relative probability of finding a  $b$  atom at a distance  $r$  from an  $a$  atom at the origin. In a one-component system, the indices  $a, b$  disappear and only a single  $S(Q)$  and a single  $g(r)$  exist. In a system with  $n$  components, a full structural analysis requires  $n(n+1)/2$  different measurements with different coefficients in Equation 1.11: in favorable cases, this may be accomplished with the use of isotope substitution in the case of neutron diffraction,<sup>8</sup> by anomalous x-ray scattering (AXS) near an absorption edge, where the form factor has an additional component that varies rapidly with x-ray energy,<sup>9,10</sup> or by a combination of the neutron and x-ray scattering.<sup>11</sup> With a single measurement, only the average structure factor  $S(Q)$  can be determined; nevertheless, this may still contain useful information. For example, if a particular peak  $n$  in  $g(r)$  can be associated uniquely with a coordination shell for a pair of atom types  $a, b$ , the coordination number of  $b$  atoms about an average  $a$  atom for that shell is given by

$$C_a^n(b) = \frac{c_b}{W_{ab}} \int_n r T(r) dr, \quad (1.12)$$

where  $T(r) = 4\pi\rho_0 r g(r)$  and the integral is taken over the peak  $n$ , while the centroid of  $T(r)$  over the same peak gives the average coordination distance  $r_{ab}^n$ .

In a magnetic system, neutrons can also scatter from the magnetic moments associated with the unpaired electrons. In simple cases where the unpaired

electrons can be associated with a particular atom, the magnetic scattering can be described by making the substitution

$$b_a \rightarrow g_n r_0 f_{ma}(Q) \frac{1}{2} g_a \mathbf{S}_a \quad (1.13)$$

in the formalism given above, where  $g_n = -1.9132$  is the g-factor for the neutron,  $r_0 = 2.8179$  fm is the classical radius of the electron, and  $f_{ma}(Q)$ ,  $g_a$ , and  $\mathbf{S}_a$  are the magnetic form factor, g-factor, and spin operator of the unpaired electrons on the atoms of element  $a$ . It is clear that if there are correlations between the orientations of the magnetic moments in the system with their positions, i.e., some kind of magnetic ordering, there will be a structure-dependent term in the magnetic scattering analogous to the first term in the expression for the nuclear scattering, Equation 1.6. If, on the other hand, the orientations of the magnetic moments are completely random, as in a paramagnetic system, the magnetic scattering is independent of the structure and can be described by a term

$$\frac{2}{3} |g_n r_0 f_{ma}(Q)|^2 \langle \mu_a^2 \rangle \quad (1.14)$$

analogous to the second term in Equation 1.6,  $\bar{\mu}_a = 1/2 g_a \bar{S}_a$  being the magnetic moment of the  $a$ th atom.

It is clear from the Fourier transform in Equation 1.10 that long-range structural information will tend to dominate the scattering at low  $Q$  and short-range at high  $Q$ . Thus, the need to get accurate information about nearest-neighbor correlations, such as bond distances and coordination numbers, has driven the development of diffractometers with a large  $Q$  range, exploiting epithermal neutrons from pulsed spallation sources and high-energy x-rays from third-generation synchrotron sources.

### 1.2.2 Differences between Neutron and X-Ray Scattering

Experimentally, a significant difference is that x-rays with energies available in a laboratory source or in a typical synchrotron beam are more highly absorbing than neutrons, which must be taken into account when designing sample containers and environmental equipment. With the x-ray energies on the order of 100 keV available from third-generation synchrotron sources, the absorption is much less significant. Other differences include the following:

1. Since the form factors depend on  $Q$  and fall off as  $Q$  increases, measurements at high  $Q$  values (e.g., beyond  $5 \text{ \AA}^{-1}$ ) become more difficult. Also, the  $Q$  dependence has to be taken into account when calculating structure factors as in Equation 1.6. This is a significant problem when the sample has more than one atom.

2. Since the form factors are not significantly isotope dependent, the scattering is always coherent in the sense used in neutron scattering.
3. Form factors are not generally energy dependent but have a strong energy variation near an absorption edge, as well as an imaginary component. This behavior is called *anomalous scattering* and can be exploited to distinguish scattering from a specific element, somewhat like isotope substitution in the neutron case.
4. Since x-ray energies of 10 keV and higher must generally be used to get an adequate  $Q$  range for studies of atomic structure and dynamics, it is difficult to get energy resolution in inelastic x-ray scattering (IXS) comparable to that obtainable in INS. At present the limit is about 1 meV. A compensating advantage is that the velocity of x-rays is orders of magnitude higher than any sound velocity in condensed matter, so that the kinematic restrictions that make it hard to make dynamical measurements at low  $Q$  and high  $E$  with INS do not apply.<sup>4</sup>
5. X-rays do not have a magnetic moment and so the interaction with magnetic moments in condensed matter is much weaker. On the other hand, polarization of an x-ray beam can be exploited for magnetic studies, as in magnetic circular dichroism, for example.

These examples show that neutrons and x-rays have many complementary features, and it is often important to use both techniques, as well as others described below, to investigate a complex material or phenomenon.

### 1.2.3 Selected Example

An example of a diffraction measurement on a material confined in a porous host is the study of highly loaded Se in a  $\text{Cu}^{2+}$  ion-exchanged Y zeolite<sup>12</sup> by AXS,<sup>10</sup> which was complemented by diffuse reflectance and Raman spectroscopy measurements. The diffraction measurements were made at two energies, 20 and 300 eV below the K absorption edge of Se at 12,658 eV. Near an absorption edge of an element  $a$ , the scattering factors

$$f_a(Q, E) = f_{a0}(Q) + f'_a(Q, E) + i f''_a(Q, E) \quad (1.15)$$

are complex with anomalous terms that vary strongly with energy. Accordingly, the weighting factors  $W_{aj}$  involving the element  $a$  in the x-ray analogue of Equation 1.11 can be altered by tuning the x-ray energy near the absorption edge. From measurements at two energies below that edge, the difference structure factor  $S_a(Q)$  associated with the element can be derived from the relation

$$I(Q, E_1) - I(Q, E_2) = 2c_a \Delta f'_a \langle f(Q) \rangle [S_a(Q) - 1] + 2c_a \Delta f''_a f_a(Q). \quad (1.16)$$

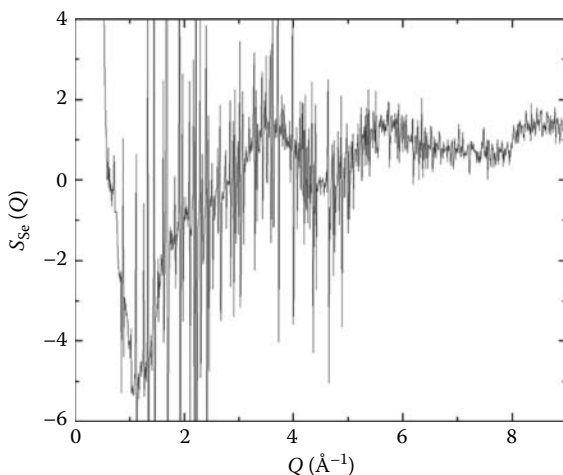


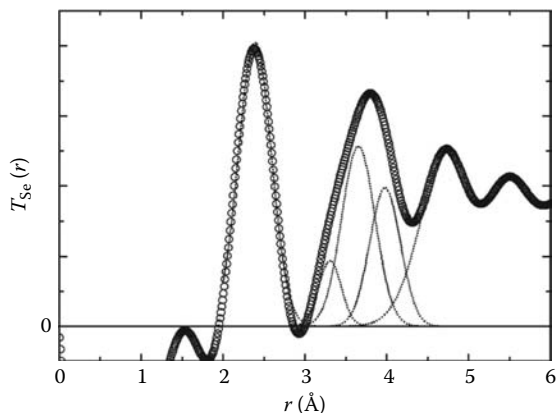
**FIGURE 1.5**

Difference structure factor  $S_{\text{Se}}(Q)$  of Cu-Y zeolite loaded with 12.5 Se per supercage derived from two diffraction experiments at 20 and 300 eV below the K absorption edge of selenium. (With permission from Goldbach, A., Saboungi, M.-L., Iton, L.E., and Price, D.L., Approach to band-gap alignment in confined semiconductors, *J. Chem. Phys.*, 115, 11254, 2001.)

The difference pair correlation function  $g_a(r)$  can be obtained by Fourier transformation of  $S_a(Q)$ , through a relation analogous to Equation 1.10.

Figure 1.5 shows the difference structure factor  $S_{\text{Se}}(Q)$  determined from the diffraction experiments at the two energies, corrected for resonant Raman scattering, dead-time effects, Compton scattering, multiple scattering, and absorption in the sample. It can be seen to consist of a smoothly varying diffuse component with sharp positive and negative spikes superimposed on it. The diffuse component arises from the encapsulated Se, estimated from weight balance to amount to about 12.5 Se atoms per zeolite supercage. The sharp spikes result from a slightly imperfect cancellation of the large Bragg scattering from the zeolite host in the difference of the two measurements. The fact that the Se scattering is diffuse instead of following the Bragg peaks of the zeolite host shows that the Se atoms have a disordered structure, out of registry with the crystalline lattice of the zeolite host.

Figure 1.6 shows the corresponding pair correlation function in real space. For technical reasons, the function  $4\pi\rho_0g_a(r)$  was used in the analysis rather than  $g_a(r)$  itself. The spikes that appeared in  $S_{\text{Se}}(Q)$  due to the imperfect cancellation of the zeolite Bragg peaks do not lead to any observable peaks in  $T_{\text{Se}}(r)$  because of their very low weight. The oscillations below 2 Å are due to truncation effects caused by the limited  $Q$  range of the  $S_{\text{Se}}(Q)$  measurement. The distinguishable peaks in the region above 2 Å were fitted with Gaussian functions. The first peak centered at  $R_{\text{SeSe}}(1) = 2.39 \pm 0.02$  Å reflects the intramolecular Se correlation. This distance is significantly longer than the

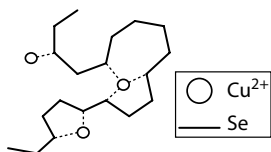


**FIGURE 1.6**

Difference pair correlation function  $T_{\text{Se}}(r)$  calculated from the difference structure factor displayed in Figure 1.5. (With permission from Goldbach, A., Saboungi, M.-L., Iton, L.E., and Price, D.L., Approach to band-gap alignment in confined semiconductors, *J. Chem. Phys.*, 115, 11254, 2001.)

corresponding nearest-neighbor distances of Se encapsulates in Nd-Y, La-Y, and Ca-Y zeolites which have values ranging from 2.32 to 2.34 Å derived by a procedure identical to that used for the Cu-Y zeolite,<sup>13,14</sup> pointing to a weakening of the intrachain bonding in comparison to other zeolites. Except for trigonal Se, it also exceeds the values found in bulk Se forms, 2.336 Å in monoclinic Se and 2.356 Å in amorphous Se. The second peak extends between 3.0 and 4.5 Å and contains three types of correlations: secondary Se–Se correlations, Se–O encapsulate framework interactions, and Se–Cu<sup>2+</sup> pairs. Since the three Gaussian functions fitted to this peak are not completely resolved, the corresponding distances were assigned with significant error bars:  $R_{\text{SeSe}}(2) = 3.65 \pm 0.10$  Å,  $R_{\text{SeO}} = 3.95 \pm 0.05$  Å, and, for the small first component,  $R_{\text{SeCu}} = 3.30 \pm 0.05$  Å. This last component was not observed in the other zeolite studies just mentioned. While it was not possible to obtain absolute coordination numbers from these data, the areas of the peaks at  $R_{\text{SeSe}}(1)$  and  $R_{\text{SeSe}}(2)$  were similar, as expected for isolated rings or extended chains, suggesting that intermolecular Se–Se interactions play a minor role in this material as in the other zeolites.

The results presented here, together with the complementary Raman scattering measurements, indicated significant interactions between the incorporated Se and the Cu–Y matrix that modify the semiconductor's electronic structure. The absence of Raman bands characteristic of Se<sub>8</sub> rings suggested the formation of long Se chains inside the voids of the zeolite. The similarity of the values of the peak areas around  $R_{\text{SeSe}}(1)$  and  $R_{\text{SeSe}}(2)$  in the AXS measurement showed that these chains are mostly isolated. At  $R_{\text{SeSe}}(1) = 2.39$  Å the first Se–Se distance is extraordinarily large for a covalent Se bond which points to a weakening of the intrachain bonding in comparison to

**FIGURE 1.7**

Schematic illustration of bonding situations between the encapsulated Se and the metal cations in Cu-Y zeolite.

the structure of Se chains in the other zeolites. This conclusion is corroborated by the large red shift of the encapsulate Raman band, while the width of this feature implies strong irregularities within the Se chains. Altogether, these features point to a new type of interaction between the encapsulated Se and the  $\text{Cu}^{2+}$  ion. This interaction was identified with the short-range correlation at  $3.30 \text{ \AA}$ , which did not appear in the pair distribution functions obtained for other Se zeolite encapsulates. The authors concluded that  $\text{Cu}^{2+}$  ions could be coordinated to one, two, or even more Se atoms of chain

fragments of various length and that these distinct bonding situations could randomly alternate along the chain, as shown schematically in Figure 1.7.

This study demonstrated the possibility of cation-directed band-gap alignments in zeolite-encapsulated semiconductors and established a convenient method for adjusting the electronic levels of clusters and molecules hosted in molecular sieves, which may be expedient for potential technical devices such as lasers or sensors.

---

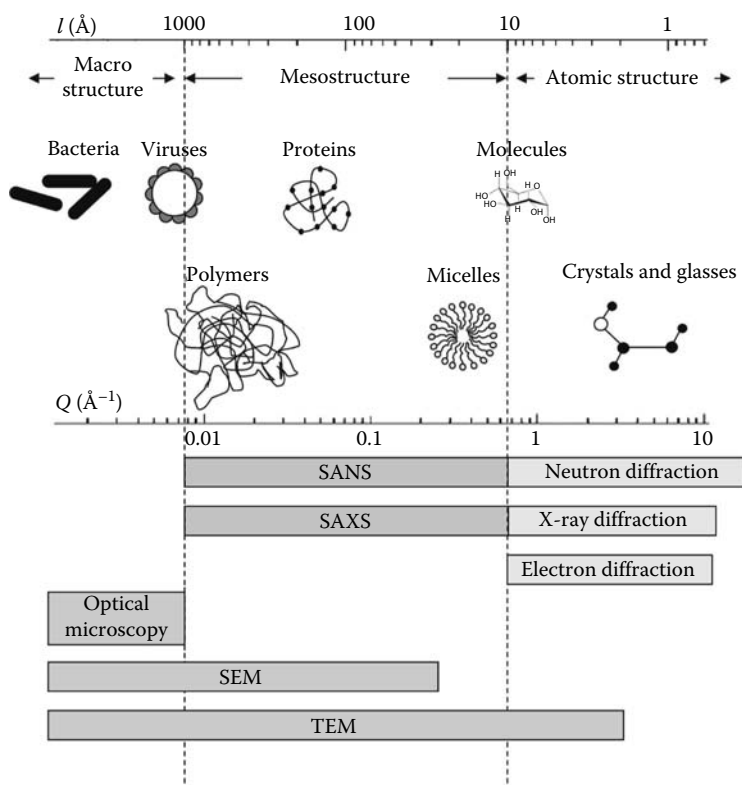
## 1.3 Small-Angle Scattering

SAS is a nondestructive technique and a very effective probe to study geometry and texture of inhomogeneities in the mesoscopic and macroscopic range, i.e., between  $5$  and  $500 \text{ nm}^*$  according to the IUPAC definition.<sup>15–18</sup> Because of the size range explored, SAS is a perfect complement of scanning and transmission electron microscopy (SEM, TEM) as well as diffraction (Figure 1.8). Small-angle neutron scattering (SANS) and its x-ray analog (SAXS) can be extremely useful in biology, polymer science, materials science, and chemistry. In this case the weaker scattering power gives the neutron measurements an advantage, since the samples are usually of manageable size— $1$ – $2 \text{ mm}$  thick. Another advantage is that, as we will see later, contrast matching is much easier with neutrons, especially in systems containing light elements and in particular hydrogen atoms.

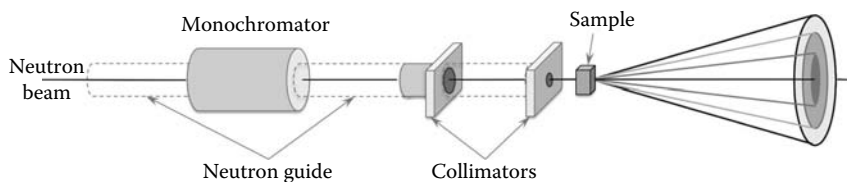
### 1.3.1 SAS Spectrometer

A SANS spectrometer is composed first of a monochromator capable of selecting wavelengths  $\lambda_0$  in the range  $5$ – $20 \text{ \AA}$ , followed by several diaphragms (collimators) used to produce a parallel beam (Figure 1.9). The scattered neutrons

\* The corresponding scattering vector range is approximately  $10^{-3} < Q < 0.1 \text{ \AA}^{-1}$ .

**FIGURE 1.8**

Examples of structures whose size range is between 1 and  $10^4$  Å (0.1 nm–1  $\mu\text{m}$ ). The complementarities of SANS and SAXS with x-ray, neutron, and electron diffraction and electron microscopies (SEM and TEM) are shown in the lower part of the figure.

**FIGURE 1.9**

Schematic representation of a small-angle scattering spectrometer.

resulting from the interaction of neutrons with the sample are collected on a 2D receptor plate, which counts the number of neutrons  $C$  as a function of the scattering angle  $\Delta\Omega$  and, if desired, the azimuthal angle. The detector is placed far enough from the sample, typically 1–15 m, in order to collect data at small angles ( $\theta < 4^\circ$ ).

### 1.3.2 Small Angle Scattering vs. Diffraction

For classical Bragg diffraction, an intense peak is observed when Bragg's law is fulfilled, i.e., when  $n\lambda_0 = 2d \sin \theta$ , where  $d$  is the distance between crystallographic planes,  $\lambda_0$  the wavelength of the incident beam, and  $2\theta$  the scattering angle. In the case of periodic inhomogeneities with period  $d$ , the scattering peaks occur at angles where the scattering vector<sup>19</sup>  $Q = 4\pi \sin \theta / \lambda_0 = 2\pi n / d$ . In order to study objects of a size scale in the range 50–5000 Å, it is important to work at low  $Q$  values requiring low scattering angles  $2\theta$  (typically  $< 4^\circ$ ) and long-wavelength or “cold” neutrons (typically  $\lambda > 4 \text{ \AA}$ ). For crystalline samples the use of long wavelength has the additional advantage of avoiding multiple processes involving Bragg reflections.

### 1.3.3 What Does $Q$ Probe?

By definition,  $Q$  and  $d$  are inversely proportional. Thus, probing a particular  $Q$  range is equivalent to taking pictures of the sample at different levels of magnification (Figure 1.10).

For high  $Q$  values, the window of observation is so tiny that no contrast variation is observable. It corresponds roughly to the molecular scale, and, in some particular cases, such as crystals or organized materials, sharp diffraction peaks can be observed in this domain. At lower  $Q$ , a difference in contrast is observable at interfaces: this is the *Porod domain*, generally exhibiting a  $Q^{-4}$  dependence of the intensity, corresponding to a sharp discontinuity between two media. At still lower  $Q$ , the total intensity is representative of the shape of the scattering entities and can show an overall dependence ranging from  $Q^{-1}$  to  $Q^{-4}$ , depending on the shape. At very low  $Q$  values, the window is now large enough to probe the structural arrangement of the scattering entities (Figure 1.10). A careful study of the intensity as a function of  $Q$  allows us to determine two important quantities: the *form factor*  $P(Q)$  that depends on the scattering entities, and the *structure factor*  $S(Q)$  that

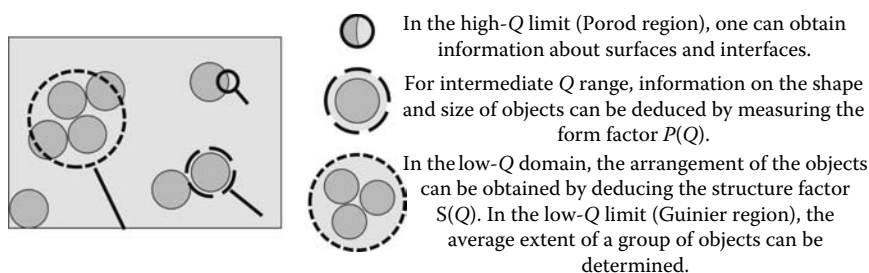


**FIGURE 1.10**

Schematic representation of spherical objects embedded in a uniform matrix probed at three different values of the scattering vector  $Q$ .

depends on the arrangement. We will now give explicit forms for these two functions.

### 1.3.4 Small-Angle Scattering Formalism

During a SANS experiment, the sample is exposed to a neutron beam and the scattered neutrons are counted as a function of the scattering angle and can be expressed as

$$C = \Phi \Delta\Omega A \eta T d \frac{d\Sigma}{d\Omega}(\vec{Q}), \quad (1.17)$$

where

$C$  is the count rate

$\Phi$  is the incident neutron flux

$\Delta\Omega$  is the considered solid angle

$A$  is the area of the sample exposed to the beam

$\eta$  is the efficiency of the detector

$T$  is the transmission of the sample

$d$  is the thickness of the sample

$\frac{d\Sigma}{d\Omega}(\vec{Q}) = \frac{N}{V} \frac{d\sigma}{d\Omega}(\vec{Q}) = \frac{1}{V} \left| \sum_{i=1}^N b_i e^{i\vec{Q}\vec{r}_i} \right|^2$  is the *macroscopic differential scattering*

*cross section* summed over all  $N$  atoms in a volume  $V$  of the sample.

$V$  is the volume of the sample

$N$  is the number of atoms (scatterers)

The aim of the experiment is to determine the differential scattering cross section per atom, which contains all the information on shapes, sizes, and interactions between the scattering entities. In SAS experiments, it is more natural to think in terms of material properties rather than atomic properties, so it is legitimate to define a *scattering length density*  $\rho$  (SLD)<sup>20–24</sup>:

$$\rho = \frac{\sum_{i=1}^N b_i}{V}. \quad (1.18)$$

By replacing the sum over  $N$  atoms with integral over the volume  $V$ , we obtain the Rayleigh–Gans equation<sup>25</sup>

$$\frac{d\Sigma}{d\Omega}(\vec{Q}) = \frac{1}{V} \left| \int_V \rho(\vec{r}) e^{i\vec{Q}\vec{r}} d\vec{r} \right|^2. \quad (1.19)$$

In a medium containing relatively heavy particles in comparison with the neutron mass, the elastic and quasi-elastic scattering, for which  $|k_i| = |k_f| = 2\pi/\lambda$ , are predominant.<sup>26–29</sup> In this static approximation, one can write

$$\frac{d\Sigma}{d\Omega}(\vec{Q}) = \frac{1}{V} \left\langle \left| \int_V \rho(\vec{r}) e^{i\vec{Q}\vec{r}} d\vec{r} \right|^2 \right\rangle, \quad (1.20)$$

where the brackets  $\langle \dots \rangle$  signify an average over all the atoms.

In general terms, the scattering length  $b_i$  depends on both the isotopic state of the nucleus and its spin state. It is then convenient, as in Section 1.2.1, to split the differential scattering cross section per unit volume into two terms containing the coherent and incoherent scattering, respectively:

$$\frac{d\Sigma}{d\Omega}(\vec{Q}) = \left( \frac{d\Sigma(\vec{Q})}{d\Omega} \right)^{\text{coh}} + \left( \frac{d\Sigma(\vec{Q})}{d\Omega} \right)^{\text{inc}}, \quad (1.21)$$

where

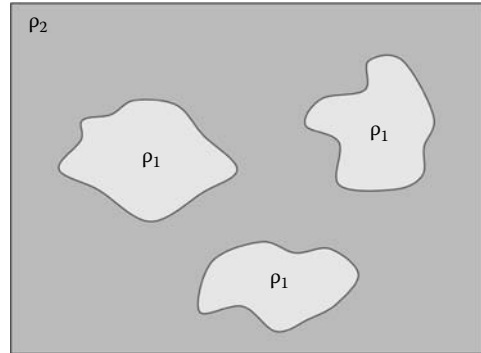
$$\left( \frac{d\Sigma(\vec{Q})}{d\Omega} \right)^{\text{coh}} = \frac{1}{V} \left\langle \left| \sum_{i=1}^N \bar{b}_i e^{i\vec{Q}\vec{r}_i} d\vec{r} \right|^2 \right\rangle \quad \text{and} \quad \left( \frac{d\Sigma(\vec{Q})}{d\Omega} \right)^{\text{inc}} = \frac{1}{V} \sum_{i=1}^N (\bar{b}_i^2 - \bar{b}_i^2).$$

The coherent scattering, which is directly related to the spatial distribution of atoms in the sample, gives information on the structure and size of inhomogeneities, while the incoherent scattering gives a flat background independent of  $Q$ .

### 1.3.5 SAS from a Two-Phase System

We consider a two-phase system composed of particles of uniform SLD  $\rho_1$  embedded in a matrix of uniform SLD  $\rho_2$  (Figure 1.11). Each phase is supposed to be incompressible in such a way that the total volume of the sample  $V$  is the sum of the respective sub-volumes  $V_1$  and  $V_2$  of the two considered phases 1 and 2. Then, the Rayleigh–Gans equation becomes

$$\frac{d\Sigma(\vec{Q})}{d\Omega} = \frac{1}{V} \left| \int_{V_1} \rho_1 e^{i\vec{Q}\vec{r}} d\vec{r}_1 + \int_{V_2} \rho_2 e^{i\vec{Q}\vec{r}} d\vec{r}_2 \right|^2, \quad (1.22)$$

**FIGURE 1.11**

Example of a sample composed of two incompressible phases of scattering length density  $\rho_1$  and  $\rho_2$ .

where  $V = V_1 + V_2$ . Equation 1.22 can then be rearranged as

$$\frac{d\Sigma(\vec{Q})}{d\Omega} = \frac{1}{V} \left| \rho_1 \int_{V_1} e^{i\vec{Q}\vec{r}} d\vec{r}_1 + \rho_2 \left( \int_V e^{i\vec{Q}\vec{r}} d\vec{r} - \int_{V_1} e^{i\vec{Q}\vec{r}} d\vec{r}_1 \right) \right|^2. \quad (1.23)$$

At nonzero  $Q$  values, this reduces to

$$\frac{d\Sigma(\vec{Q})}{d\Omega} = \frac{1}{V} (\rho_1 - \rho_2)^2 \left| \int_{V_1} e^{i\vec{Q}\vec{r}} d\vec{r}_1 \right|^2, \quad (1.24)$$

$(\rho_1 - \rho_2)^2$  is the so-called *contrast factor* which is an intrinsic property of the material (density, composition). The integral term is indicative of the spatial arrangement of phase 1.

Equation 1.24 shows that  $d\Sigma/d\Omega$ , and hence  $I(\vec{Q})$ , is proportional to  $(\rho_1 - \rho_2)^2$ . Consequently, the higher the contrast factor is, the more intense will be the coherent scattering signal. Moreover, since the contrast factor is the square of the difference in SLD between the particles and the matrix, two homologous structures with reversed SLD will show identical coherent scattering profiles according to Babinet's Principle (Figure 1.12). This property is related to the fact that  $d\Sigma/d\Omega$  is proportional to the square of an amplitude, leading to an unavoidable loss of phase information. In the limiting case where the two phases have identical SLD, i.e., when the contrast factor is equal to zero, no coherent scattering is observable since the sample appears homogeneous toward the neutron beam. These properties turn out to be very efficient in the determination of partial structures in multiphase systems.

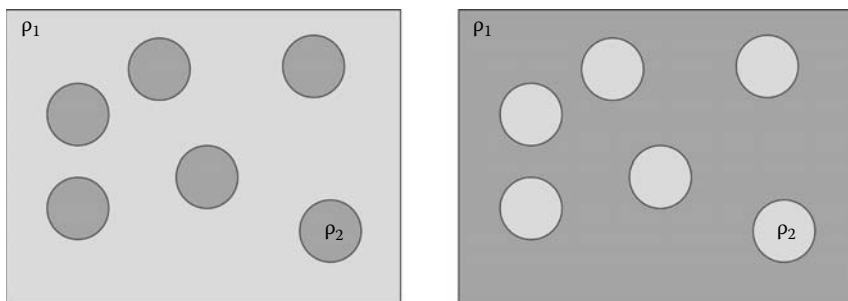


FIGURE 1.12

Babinet's principle: two identical structures with reversed scattering length densities will give the same coherent scattering.

In a *dilute medium*, i.e., when one phase consists of  $N_p$  identical particles sufficiently far enough to neglect interparticle interaction between them, Equation 1.24 can be considerably simplified:

$$\frac{d\Sigma(\vec{Q})}{d\Omega} = \frac{N_p}{V} (\rho_1 - \rho_2)^2 \left| \int_{V_p} e^{i\vec{Q}\vec{r}} d\vec{r} \right|^2 = n_p (\rho_1 - \rho_2)^2 V_p^2 P(\vec{Q}), \quad (1.25)$$

where

$$P(\vec{Q}) = \frac{1}{V_p^2} \left| F(\vec{Q}) \right|^2 = \frac{1}{V_p^2} \left| \int_{V_p} e^{i\vec{Q}\vec{r}} d\vec{r} \right|^2. \quad (1.26)$$

Here  $n_p = N_p/V$  and  $V_p$  represent the number density of the particles and the volume of each particle, respectively. The scattering amplitude  $F(\vec{Q})$  contains all the information about the shape of the particles.  $P(\vec{Q})$  is commonly called the *form factor* and represents the interference of neutrons scattered from different parts of the same object. In the limiting case where  $Q \rightarrow 0$ , Equation 1.25 reduces to

$$\frac{d\Sigma}{d\Omega} \xrightarrow{Q \rightarrow 0} n_p V_p^2 (\rho_1 - \rho_2)^2, \quad (1.27)$$

so that the intensity as  $Q \rightarrow 0$  can be used to measure the volume of the scattering particle  $V_p$  or its molecular weight  $M_w = \rho V_p N_A$  if its chemical composition and density are known.

### 1.3.5.1 Guinier Approximation: Radius of Gyration

In the approximation of small  $Q$  values such that  $Ql \ll 1$ , where  $l$  is a characteristic particle size, a development of the form factor in Taylor series and a reinterpretation in terms of an exponential leads to the *Guinier law*:

$$P(\vec{Q}) = F^2(Q) = e^{-\frac{(QR_g)^2}{3}} \quad (QR_g < 1), \quad (1.28)$$

where  $R_g$  is the *Guinier radius* corresponding to the root-mean-square extension of the particle from its center of scattering density. For a homogeneous particle this is equivalent to the *radius of gyration* given by

$$R_g^2 = \frac{\int V_P r^2 d\vec{r}}{V_P}. \quad (1.29)$$

Knowing that the relative scattering intensity  $I(Q) \propto P(Q)$ , Equation 1.28 can be formulated in a different way:

$$I(Q) = I(0)e^{-\frac{(QR_g)^2}{3}} \quad (1.30)$$

$$\ln(I(Q)) = \ln(I(0)) - \frac{(QR_g)^2}{3}. \quad (1.31)$$

Using Equation 1.31, it is possible to evaluate the radius of gyration  $R_g$  of the scattering entity from the experimental data by plotting  $\ln(I(Q))$  vs.  $Q^2$ . The Guinier law is a powerful equation to characterize soft matter and more particularly polymers, but it has to be used with caution since the approximation is valid only in dilute systems composed of isotropic particles under the condition  $QR_g \ll 1$ .

Some examples of radius of gyration for some usual homogeneous particles are given below<sup>30,31</sup>:

---

|  |   |
|--|---|
| Sphere of radius $R$                   | $R_g^2 = \frac{3R^2}{5}$                                  |
| Spherical shell with radii $R_1 > R_2$ | $R_g^2 = \frac{3}{5} \frac{R_1^5 - R_2^5}{R_1^3 - R_2^3}$ |
| Ellipse with semiaxes $a$ and $b$      | $R_g^2 = \frac{a^2 + b^2}{4}$                             |
| Ellipsoid with semiaxes $a, b, c$      | $R_g^2 = \frac{a^2 + b^2 + c^2}{5}$                       |

|   |  |
|---|--|
| Prism with edges $A, B, C$                                | $R_g^2 = \frac{A^2 + B^2 + C^2}{12}$     |
| Cylinder with radius $R$ and length $l$                   | $R_g^2 = \frac{R^2}{2} + \frac{l^2}{12}$ |
| Gaussian coil of root-mean-square end-to-end distance $L$ | $R_g^2 = \frac{L^2}{6}$                  |

---

### 1.3.5.2 Porod Scattering

Where as the Guinier approximation considers the low- $Q$  limit of SAS, the high- $Q$  limit can be described using an approximation due to Porod. At high values of  $Q$ , i.e., when  $Q \gg 1/l$  where  $l$  is the size of the scattering object, the scattering intensity is dominated by the signal coming from the boundaries between the phases of the system. The interface appears as a discontinuity of the SLD leading to the following expressions:

$$I(Q) \propto Q^{-4}, \quad (1.32)$$

and, more specifically,

$$\frac{4\pi^2}{\tilde{Q}} \lim_{Q \rightarrow \infty} \left( \frac{d\Sigma}{d\Omega}(Q)Q^4 \right) = \frac{S}{V}, \quad (1.33)$$

where  $\tilde{Q}$  is the *scattering invariant*, i.e., the integral of the macroscopic cross section over  $\tilde{Q}$ , and  $S/V$  is the *specific surface* corresponding to the total area of interface per unit volume of the sample. The determination of the total specific surface by SAS, whatever the size and shape of the particle, turns out to be useful in the characterization of porous materials and can be an excellent complement to adsorption measurements such as BET since neutron or x-ray beam probes the overall interface surface whereas adsorption is limited to surfaces accessible to the molecules of the working gas.

### 1.3.5.3 Porod Invariant

In 1952, Porod demonstrated that the total SAS from a sample, which depends on both the contrast and volume fraction, is constant and independent of the dispersion of scattering entities. The *scattering invariant* or *Porod invariant* is representative of the total amount scattered, but not of the detailed structure. By integrating the scattering intensity with respect to  $\tilde{Q}$ , we can demonstrate that in the case of an incompressible two-phase system

$$\tilde{Q} = (2\pi)^3 \phi_1(1 - \phi_1)(\rho_1 - \rho_2)^2$$

$$\tilde{Q} \approx (2\pi)^3 \phi_1 (\rho_1 - \rho_2)^2 \quad \text{if } \phi_1 \ll 1, \quad (1.34)$$

where  $\phi_1 = n_p V_p$  is the volume fraction of the particles.

For uncorrelated particles, Equations 1.27 and 1.34 give access to the volume fraction of particles and consequently to the volume of each particle:

$$V_p = \frac{(2\pi)^3}{\tilde{Q}} \frac{d\Sigma}{d\Omega}(0). \quad (1.35)$$

We note that in Equations 1.33 and 1.35 the measured intensity appears in both numerator and denominator, so considerable information can be obtained from measurement of the relative intensity  $I(Q)$ , without the need for absolute normalization, as long as the  $Q$  range is sufficient to obtain accurate values for the integrated intensity and the low- and high- $Q$  limits (not always an easy condition to obtain in practice).

### 1.3.6 Form Factors

Experimentally, form factors and scattering amplitudes can only be measured directly in the dilute regime where particles are considered as independent and noninteracting. The precise form of  $F(\vec{Q})$  depends on the shape and orientation of the scatterer. Isotropic spherical particles represent the simplest case since considerations about particle orientation do not arise. In the case of an ideal spherical particle of radius  $R$  and of uniform SLD  $\rho_1$ , the form factor can be simply expressed as follows:

$$P(Q) = \left( \frac{3(\sin QR - QR \cos QR)}{(QR)^3} \right)^2. \quad (1.36)$$

If the particle morphology is not spherical, the orientation relative to the scattering vector  $\vec{Q}$  must be considered in the evaluation of  $P(\vec{Q})$ . In the general case, i.e., for particles of arbitrary shape and with no preferential orientation, the form factor has to be averaged over all the orientations taken by the different scatterers:

$$\overline{P(Q)} = \overline{F_i^2(Q)} = \int_0^1 |F_i(Q, \mu)|^2 d\mu, \quad (1.37)$$

where  $\mu = \cos \alpha$  and  $\alpha$  is the angle between an axis of the scatterer and  $\vec{Q}$ . Form factors of common shapes can be found in the literature.<sup>30</sup> Nonetheless, we give the form factors for two usual geometries:

- For long cylinders of radius  $R$  with a length  $L$

$$\overline{P(Q)} = \left[ \frac{2}{(QL)} \left( \int_0^{QL} \frac{\sin u}{u} du \right) - \frac{\sin^2 \frac{QL}{2}}{\left( \frac{QL}{2} \right)^2} \right], \quad (1.38)$$

- For thin disks of radius  $R$

$$\overline{P(Q)} = \frac{2}{(QR)^2} \left[ 1 - \frac{1}{2QR} J_1(2QR) \right], \quad (1.39)$$

where  $J_1(x)$  is the first-order Bessel function.

At intermediate values of  $Q$ ,  $P(Q)$  varies as  $1/Q$  in the case of a cylindrical shape and as  $1/Q^2$  for thin disks (Figure 1.13). This tendency can be expressed as a more general rule: there exists a range of  $Q$  for which the measured scattering intensity  $I(Q)$  will vary as  $1/Q$  for one-dimensional objects (narrow

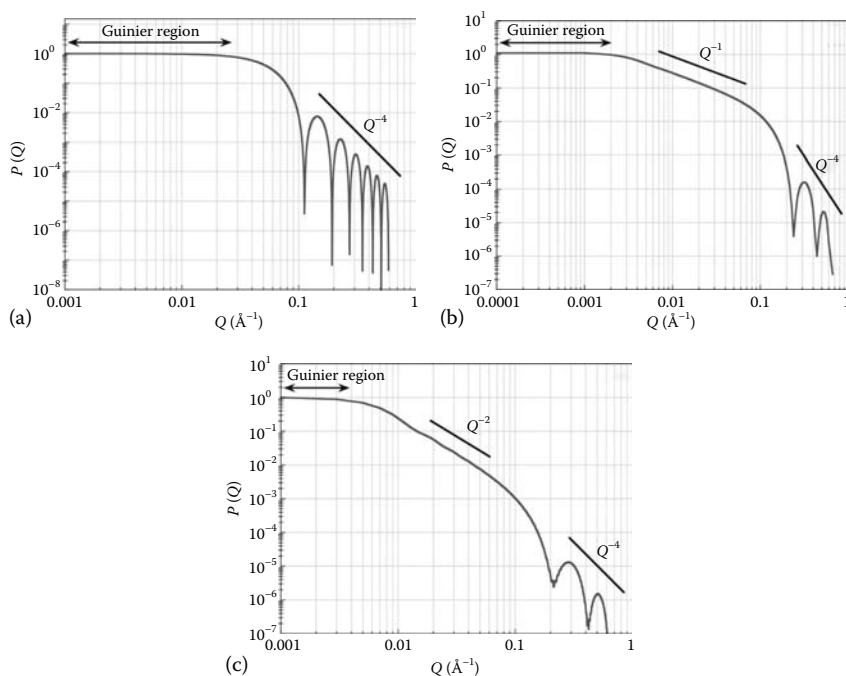


**FIGURE 1.13**

Form factors of three usual shapes: (a) spheres ( $R=40 \text{ \AA}$ ), (b) cylinders ( $R=60 \text{ \AA}$ ,  $L=34 \text{ \AA}$ ), and (c) thin disks ( $R=300 \text{ \AA}$ , thickness= $30 \text{ \AA}$ ). (From Kline, S.R., *J. Appl. Cryst.*, 39, 895, 2006.)

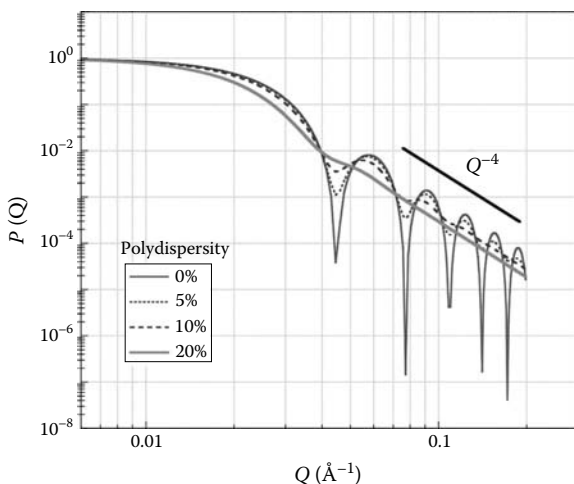


**FIGURE 1.14**

Evolution of the form factor of solid hard spheres ( $R = 100 \text{ \AA}$ ) as a function of the polydispersity of the radius.

cylinders, wires, ...) and as  $1/Q^2$  for 2D objects (thin disks, platelets, ...). Such dependencies can be graphically detected by plotting  $\log I(Q)$  vs.  $\log(Q)$ .

The above form factors represent the ideal sample for which the shape and size of particles are perfectly controlled. It is noteworthy that, as good as the synthesis methods are, this perfect scenario is far from the reality, and there are generally distributions in both size and shape. In this case, the form factor has to be averaged over the size distribution leading to a smearing of the principal features. An example of the effect of polydispersity on the global shape of the form factor of solid hard spheres is shown in Figure 1.14.

### 1.3.7 Multicomponent Systems: Neutron Contrast Matching

So far, we have assumed that our sample is constituted of a single type of particle embedded in a uniform matrix, typically a solvent. In many cases, like in biological systems or porous materials, the sample is composed of different types of subunits with different shapes and/or sizes. If two particle subunits of uniform SLD  $\rho_1$  and  $\rho_2$  give a scattering signal in the studied  $Q$  range, the measured differential cross section can be written as follows:

$$\frac{d\Sigma}{d\Omega}(\tilde{Q}) = \frac{1}{V} \left\langle \left| \int_V (\rho(r) - \rho_0) e^{i\tilde{Q}\vec{r}} d\vec{r} \right|^2 \right\rangle, \quad (1.40)$$

where  $\rho_0$  is the average SLD over the entire sample.

Knowing that  $V = V_1 + V_2$ , where  $V_1$  and  $V_2$  are the volume of the particles 1 and 2, respectively, the expression for the macroscopic cross section, which is proportional to the scattering intensity, can be rewritten as

$$\begin{aligned} \frac{d\Sigma}{d\Omega}(\vec{Q}) &= \frac{1}{V} \left\langle \left| (\rho_1 - \rho_0) \int_{V_1} e^{i\vec{Q}\cdot\vec{r}} d\vec{r}_1 + (\rho_2 - \rho_0) \int_{V_2} e^{i\vec{Q}\cdot\vec{r}} d\vec{r}_2 \right|^2 \right\rangle \\ &= \left( n_{p_1} (\rho_1 - \rho_0)^2 V_{p_1}^2 \langle |F_1(Q)|^2 \rangle + n_{p_2} (\rho_2 - \rho_0)^2 V_{p_2}^2 \langle |F_2(Q)|^2 \rangle \right), \quad (1.41) \end{aligned}$$

where  $F_a(Q)$ ,  $n_{p_a}(Q)$ , and  $V_{p_a}(Q)$  are the scattering amplitude, number density, and volume of particle type  $a$ , respectively.

It appears from Equation 1.41 that the total scattering intensity depends on both differences in SLD between the particles and the matrix,  $(\rho_1 - \rho_0)$  and  $(\rho_2 - \rho_0)$ . Consequently, it is possible to cancel one of the two terms by choosing an appropriate SLD  $\rho_0$  for the matrix (solvent). Then, two measurements are enough to obtain the parameters of interest, i.e.,  $F_1(Q)$  and  $F_2(Q)$  (Figure 1.15). In practice, SANS is more suitable than SAXS to adjust the SLDs because neutrons are very sensitive to the nature of isotopes (cf. Section 1.2). A similar adjustment can be achieved with anomalous scattering or isomorphous substitution in favorable cases. However, the latter may modify the structure of the sample. SANS is also particularly appropriate for light elements such as hydrogen for which the selective deuteration method can lead to spectacular results since the coherent scattering length of hydrogen has a different sign from that of deuterium ( $b_H = -0.374 \times 10^{-12}$  cm vs.  $b_D = 0.667 \times 10^{-12}$  cm). The H:D substitution technique has turned out to be very powerful since a simple

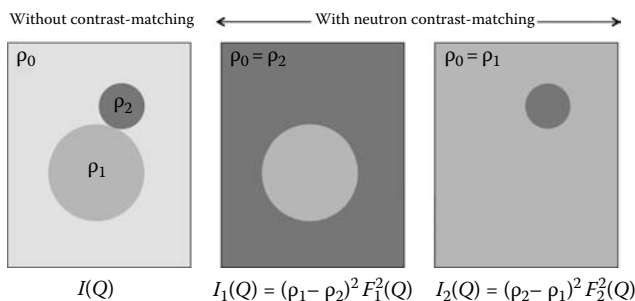


**FIGURE 1.15**

Schematic representation of the contrast-matching technique. In the present case, with only three measurements and by varying properly the scattering length density of the matrix  $\rho_0$ , it is possible to measure separately the two particle subunits. (With permission from Lelong, G., Bhattacharyya, S., Kline, S.R., Cacciaguerra, T., Gonzalez, M.A., and Saboungi, M.-L., Effect of surfactant concentration on the morphology and texture of MCM-41 materials, *J. Phys. Chem. C*, 112, 10674–10680, 2008.)

mixture of D<sub>2</sub>O with H<sub>2</sub>O is enough to match the contrast of almost every biological system and porous material.

### 1.3.8 Interacting Scatterers: Structure Factor

Up to now, we have considered the simple case of a gas of randomly dispersed particles, i.e., with no interaction between the scattering entities and no particular tridimensional arrangement. This approximation is valid for dilute systems but does not hold in the case of condensed matter or other systems with interacting particles, for which  $d\Sigma/d\Omega$  depends not only on the intraparticle structure but also on the interparticle interactions. In the case of centrosymmetric identical particles, the spatial arrangement leads to the appearance of a new function  $S(Q)$  in the expression of the coherent differential scattering cross section:

$$\frac{d\Sigma(Q)}{d\Omega} = n_p(\rho_1 - \rho_2)^2 V_p^2 P(Q)S(Q). \quad (1.42)$$

$P(Q)$  is the *form factor* that we introduced earlier and  $S(Q)$  is the *structure factor*, which represents the interference of neutrons scattered from different particles:

$$S(\vec{Q}) = \frac{1}{N_p} \left\langle \sum_{i,j=1}^{N_p} e^{i\vec{Q} \cdot (\vec{R}_i - \vec{R}_j)} \right\rangle. \quad (1.43)$$

Thus, for centrosymmetric objects, the scattering arising from one single scattering entity can be dissociated from the signal caused by the interactions between particles. For noninteracting scatterers, as in a dilute medium, one can demonstrate that  $S(Q) = 1$  over the whole  $Q$  range. In the particular case of an isotropic solution, the interparticle structure factor  $S(Q)$  can be expressed as follows<sup>33</sup>:

$$S(Q) = 1 + 4\pi n_p \int_0^{\infty} [g(r) - 1] \frac{\sin Qr}{Qr} r^2 dr, \quad (1.44)$$

where  $g(r)$  is the pair correlation function for the scattering entities and represents the probability of finding an atom at the position  $r$  assuming another at the origin. Equation 1.44 is the SAS analogy of Equation 1.10. Subsequently, the product  $n_p g(r)$  represents a local density of particles, and will be dependent on both their concentration and their spatial arrangement (Figure 1.16).<sup>33</sup>

In the case of two types of particles with correlations between all of them,  $S(\vec{Q})$  will have three partial components:

$$S_{ab}(\vec{Q}) = \frac{1}{(N_{pa}N_{pa})^{1/2}} \left\langle \sum_{i=1}^{N_{pa}} \sum_{j=1}^{N_{pb}} F_i(\vec{Q}) F_j(\vec{Q}) e^{i\vec{Q} \cdot (\vec{R}_i - \vec{R}_j)} \right\rangle. \quad (1.45)$$

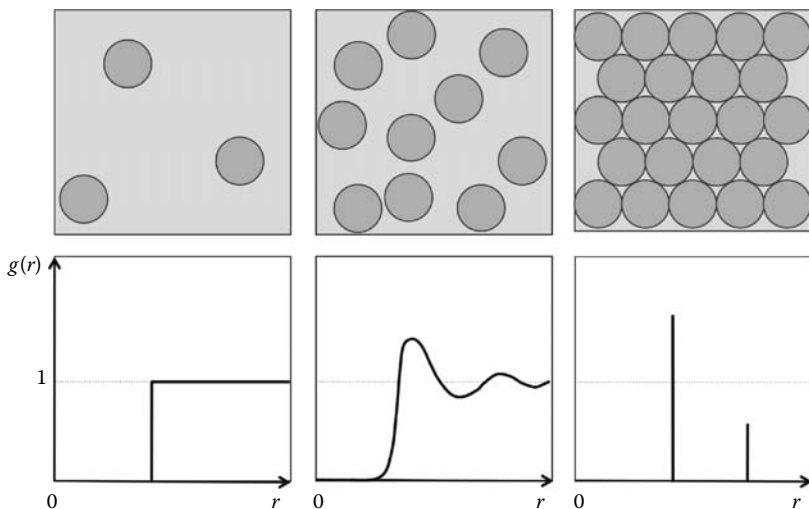


**FIGURE 1.16** Schematic representation of the pair correlation function  $g(r)$  as a function of the concentration in particles and their 3D organization (dilute, intermediate, and concentrated solutions).

and Equation 1.41 must be replaced by

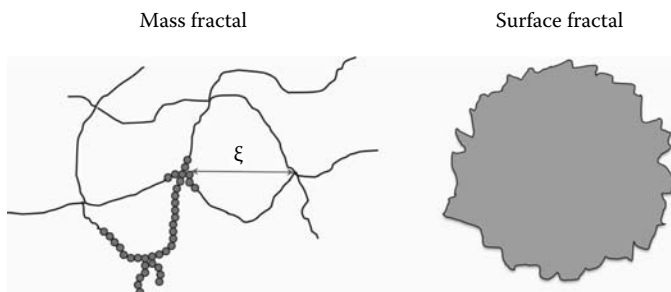
$$\begin{aligned} \frac{d\Sigma}{d\Omega}(\vec{Q}) = & \left( n_{p_1}(\rho_1 - \rho_0)^2 V_p S_{11}(\vec{Q}) + n_{p_2}(\rho_2 - \rho_0)^2 V_{p_2}^2 S_{22}(\vec{Q}) \right) \\ & + 2(n_{p_1} n_{p_2})^{1/2} (\rho_1 - \rho_0)(\rho_2 - \rho_0) V_{p_1} V_{p_2} S_{22}(\vec{Q}), \end{aligned} \quad (1.46)$$

so that three independent measurements will be needed to determine  $S_{ab}(\vec{Q})$ .

An example of a structure factor can be given in the case of fractal objects. This represent a particular class of scattering systems that have the property of self-similarity, in which a similar geometric pattern is repeated at every length scale. Two distinct classes of fractal behavior have been defined: the *mass fractal* and the *surface fractal*.<sup>34</sup> A mass fractal is a structure composed of subunits forming branching and crosslinking to create a tridimensional network, while a surface fractal is an object displaying fractal characteristics on its surface but not necessarily in its core (Figure 1.17).

In the case of mass fractals, the particle number density  $n_p$  is dependent on the position  $r$  and can be expressed as a function of the parameter  $D_m$ , the *mass fractal dimension*, generally with values in the range 2–3:

$$n_p(r) = \left( \frac{r}{r_0} \right)^{D_m}. \quad (1.47)$$

**FIGURE 1.17**

Schematic representation of the two types of fractals: (Left) The mass fractal morphology is composed of subunits of size  $r_0$  arranged in linear chains. The entanglement of the polymeric chains leads to the appearance of a correlation distance  $\xi$ . (Right) Example of surface fractal, which is characterized by a surface fractal dimension  $D_s$ .

Then, for relatively small  $Q$  values, the fractal structure factor  $S(Q)$  is given by<sup>35,36</sup>

$$S(Q) = 1 + \frac{\sin[(D_m - 1) \tan^{-1}(Q\xi)]}{(Qr_0)^{D_m}} \frac{D_m \Gamma(D_m - 1)}{\left[1 + \frac{1}{(Q\xi)^2}\right]^{\frac{D_m - 1}{2}}}, \quad (1.48)$$

where

$D_m$  is the fractal dimension

$r_0$  is the radius of the primary particles

$\xi$  is the correlation length, i.e., a characteristic size of the mass fractal

Clearly,  $S(Q)$  shows a main dependence on  $Q^{-D_m}$ . This power law decay is a clear signature of fractal objects. Using the Guinier approximation, it is possible to estimate the radius of gyration of a mass fractal knowing its fractal dimension  $D_m$  and its correlation length  $\xi$ :

$$R_g^2 = \frac{D_m(D_m + 1)\xi^2}{2}. \quad (1.49)$$

For a surface fractal, the scattering intensity has the form  $I(Q) \propto Q^{D_s - 6}$ , where  $D_s$  is the *surface fractal dimension* ranging usually from 2 for a smooth surface to 3–4 in the case of rough surfaces. When  $D_s = 2$ , the scattering intensity follows a  $Q^{-4}$  behavior, in agreement with Porod's law. Fractal dimensions larger than 4 may be found in some cases where there are no sharp interfaces but rather a gradual transition between phases.

### 1.3.9 SANS vs. SAXS

Small-angle neutron and x-ray scattering are comparable and often complementary techniques. Neutrons and x-rays interact in a different way with matter, leading to a difference in the sensitivity of both techniques: neutron scattering measures fluctuations of nuclear density, and x-rays inhomogeneities in electron density. With the use of isotopic substitution, SANS can selectively probe different species in a multicomponent system (cf. Section 1.3.7). In favorable cases, anomalous scattering, exploiting rapid variation of the x-ray form factor near an absorption edge, can be used with SAXS to distinguish different elements. Synchrotron radiation sources deliver a flux highly superior to neutron sources, favoring a fast acquisition of spectra that allows an in situ monitoring of chemical reactions or fast structural changes as a function of time. It should also be mentioned that the interaction of neutrons with unpaired spins can be used to probe magnetic inhomogeneities, for example, flux line lattices in type-II superconductors.

### 1.3.10 Selected Examples

Excellent reviews have been published in the last decade showing the main progresses of the SAS technique in a variety of domains such as magnetism,<sup>37</sup> biology,<sup>38,39</sup> polymer,<sup>40–42</sup> or material sciences.<sup>43</sup> We have selected here some examples showing the capabilities of small-angle neutron and/or x-ray scattering.

#### 1.3.10.1 Porous Materials

SAS is a natural technique characterizing mesoporous materials since their characteristic length scales are generally located in the  $Q$  window probed by SAS spectrometers. Furthermore, the richness of the accessible structural data and its complementarity with electron microscopies or adsorption methods give it a full-fledged legitimacy.

A good example is the family of mesoporous materials called MCM-41, which has been extensively studied since their discovery in the early 1990s,<sup>44</sup> and whose particle shape can be easily tailored. A recent work of Lelong et al.<sup>45</sup> demonstrates the structural evolution of mesoporous silica nanospheres as a function of the initial surfactant concentration (Figure 1.18). The spherical silica particles were composed of cylindrical pores arranged in a honeycomb structure. In view of the different particle shapes, length scales, and the two-dimensional organization of the pores, a global fit of the scattering intensity  $I(Q)$  over a large  $Q$  range is very difficult to achieve. Nevertheless, morphological and structural information were deduced from the scattering profile by using the form factors of both an ideal sphere  $P_{sphere}(Q)$  and an ideal cylinder  $P_{cyl}(Q)$ , and an appropriate structure factor  $S(Q)$ . The SANS investigation reported a decrease in the diameter of the silica particles when the surfactant

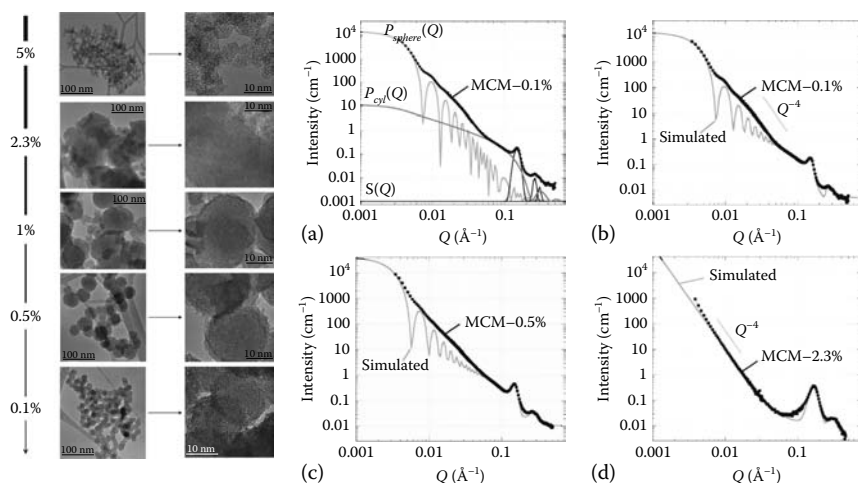


**FIGURE 1.18**

(Left) TEM images of mesoporous silica spheres as a function of surfactant concentration. (Right) (a) SANS intensity from the MCM-0.1% sample together with the form factors of a cylinder  $P_{cyl}(Q)$  and a sphere  $P_{sphere}(Q)$ . Measured and simulated SANS intensities for the (b) MCM-0.1%, (c) MCM-0.5%, and (d) MCM-2.3%. (With permission from Lelong, G., Bhattacharyya, S., Kline, S.R., Cacciaguerra, T., Gonzalez, M.A., and Saboungi, M.-L., Effect of surfactant concentration on the morphology and texture of MCM-41 materials, *J. Phys. Chem. C*, 112, 10674–10680, 2008.)

concentration was decreased accompanied by a global improvement of both the internal structure and the size dispersion. These data were corroborated by TEM pictures shown in Figure 1.18.

The determination of the total specific area is one of the major assets of SAS since it probes both the opened and closed porosities, which conventional adsorption methods do not do (cf. Section 1.3.5.2). For example, Né and Zemb<sup>46</sup> in a paper of 2003 presented a method to determine experimentally the specific area and the compaction by SAXS, if both the Porod limit and the invariant can be extracted from the scattering profile. The method was applied to a mesostructured material composed of ZrO<sub>2</sub> and a cationic surfactant (CTAB), showing a higher total interface surface and a lower compaction than in the case of crystalline ZrO<sub>2</sub>. By applying a careful methodology in the data treatment, they ascribed the origin of these significant differences to the presence of microporosities in the walls separating the mesopores. This discovery explained why this mesoporous material can collapse during removal of the template molecule at high temperature.

In the last few years, some very interesting works have been carried out on porous systems such as the study of the entanglement of labeled single-wall carbon nanotubes<sup>47</sup> to determine the global shape of aggregates, or the combination of SANS with mesoscopic simulation techniques in order to generate 2D or 3D images of the porous structure. The structural model obtained can then be used to understand the macroscopic physicochemical properties.<sup>48</sup>

The development of both high flux neutron and x-ray sources and new environmental chambers<sup>49</sup> opened the way to *in situ* SAS measurements capable of monitoring adsorption or capillary condensations for a multitude of gases.<sup>50</sup> Since the first *in situ* SAS measurements in the middle of the 1990s, many papers were devoted to the study of water or N<sub>2</sub> condensation in mesoporous materials such as Vycor, MCM-41, SBA-15, xerogels. The deformation of the pore walls and/or the pore lattice can then be followed during the intrusion of a fluid inside the mesoporosity.<sup>51,52</sup> Zickler et al. have demonstrated that the sorption of an organic fluid, perfluoropentane (C<sub>5</sub>F<sub>2</sub>), in SBA-15 is accompanied by a modification of the pore lattice as shown by the shift of the different Bragg peaks as the relative pressure is increased. A reversible deformation of the pore lattice caused by capillary stresses has also been highlighted.

In the same vein, one of the most spectacular evolutions has been the ability to carry out *in situ* time-resolved scattering experiments, opening the way to a vast field of investigation.<sup>53</sup> These new methods turn out to be fruitful in terms of information on transitory states. Fast chemical reactions can then be followed by SANS or SAXS using the *stopped-flow* method in which a small volume of reactants are mixed in a very short period of time. A remarkable example was given by Zholobenko et al.<sup>54,55</sup> who experimentally demonstrated the different stages of the *cooperative self-assembly mechanism* in the case of SBA-15 material. At the very beginning of the reaction, the template molecules (Pluronic P123) assemble into spherical micelles. In a second step, the formation of the organic-inorganic micelles is accompanied by a modification of their overall shape going from spherical to cylindrical. The aggregation of the cylindrical micelles in a 2D hexagonal structure characteristic of the mesoporous material constitutes the last step of the reaction. The void between the cylinders is then progressively replaced by silicate species to finally lead to a complete filling with further condensation (Figure 1.19).

### 1.3.10.2 Soft Matter

As mentioned earlier in the chapter, neutron scattering has the big advantage of being very sensitive to isotopic substitution. This unique property is particularly well suited to the study of soft matter, since polymers, micelles, gels, colloids, etc. are mainly composed of light elements. The contrast matching is then extensively used to disentangle complex systems.<sup>56</sup>

A good example has been given by Doe et al.,<sup>57</sup> who have fully characterized the different structures of a ternary system composed of a block copolymer (P84 – (EO)<sub>19</sub>(PO)<sub>43</sub>(EO)<sub>19</sub>), water, and *p*-xylene. Depending of the water/oil ratio, the sample can show a lamellar or a reverse hexagonal structure. A careful study of the evolution of the relative intensities of the Bragg peaks as a function of the contrast made it possible to determine the structuring in layers of the lamellar phase, and notably the presence of a water-rich layer in between the polar domains. The succession of polar and apolar subdomains has been described as follows: water rich, homogeneous PEO/water mixture,

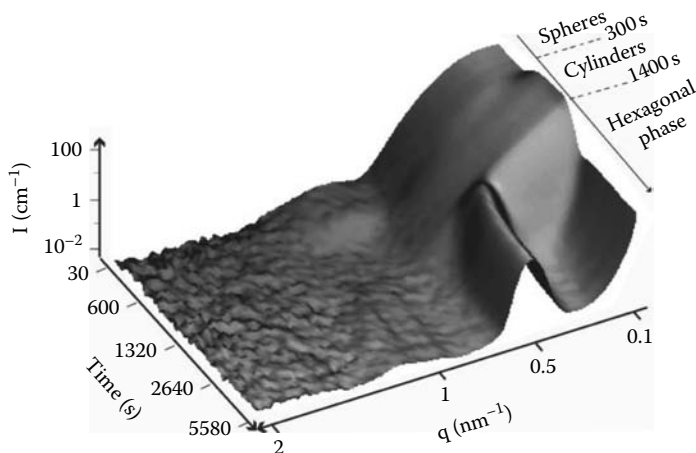


**FIGURE 1.19**

Time-resolved *in situ* SANS data for SBA-15 synthesis. (From *Adv. Coll. Interf. Sci.*, 142, Zholobenko, V.L., Khodakov, A.Y., Impéror-Clerc, M., Durand, D., and Grillo, I., Initial stages of SBA-15 synthesis: An overview, 67–74, Copyright 2008, with permission from Elsevier.)

solvent depleted, homogeneous PPO/oil mixture, solvent depleted, homogeneous PEO/water mixture, etc.

The second example deals with sugar solutions confined in silica gel.<sup>58,59</sup> The almost equal and opposite SLD of H<sub>2</sub>O ( $\rho_{\text{H}_2\text{O}} = -5 \times 10^{-7} \text{ \AA}^{-2}$ ) and D<sub>2</sub>O ( $\rho_{\text{D}_2\text{O}} = 6.36 \times 10^{-6} \text{ \AA}^{-2}$ ) makes possible the *masking* of the silica network or that of the sugar solution by using different H<sub>2</sub>O/D<sub>2</sub>O ratios. After determining the SLD of each constituent, two different gels were prepared: one to observe the silica network (*gel-silica*), and one to check the homogeneity of the sugar solution (*gel-sugar*); a sugar solution of same concentration as test sample was also prepared. The intensity profile of the *gel-silica* sample showed a  $Q^{-2}$  behavior at intermediate  $Q$  range indicative of a mass fractal object and a  $Q^{-4}$  behavior in the Porod region, typical of a smooth surface. The test solution and the *gel-sugar* sample showed the same flat intensity profile, indicative of a homogeneous repartition of the sugar molecules on the probed SANS length scale, i.e., between 3 and 100 nm. We should also mention the emergence of new studies on micelles based on rheology measurements monitored by SAS.<sup>60,61</sup>

### 1.3.10.3 New Developments

For completeness, we should mention the emergence of new *in situ* measurements coupling the SAS technique with one or two other methods of characterization. The most natural one is to use both small-angle and wide-angle x-ray or neutron scattering (WAXS or WANS) in order to increase the probed  $Q$  range, especially when objects are in a  $Q$  domain located in between SAS and diffraction. More complicated combinations can also be carried out such

as SAXS/EXAFS, SAXS/WAXS/FTIR, SAXS/WAXS/Raman, SAXS/WAXS/Light Scattering, or also SAXS/WAXS/DSC,<sup>62-64</sup> making possible the interpretation of complex phenomena.

---

## 1.4 X-Ray Absorption Spectroscopy

X-ray absorption spectroscopy is a general term referring to experiments in which the absorption of an x-ray beam by a sample is measured as a function of incoming energy. Sometimes it is more convenient to measure the fluorescence produced following the absorption rather than the attenuation of the beam. The absorption increases when the energy is raised through and above an absorption edge of one of the elements in the sample. In materials science, the important energy regions are near the edge (x-ray absorption near-edge spectroscopy, XANES) and extending for some range above the edge (EXAFS). Since the absorption edge is associated with the transition of an electron in the sample from a core level to a free state, the detailed energy dependence of the XANES spectrum gives information about the electronic structure of the valence and conduction electrons. EXAFS, on the other hand, is essentially a diffraction phenomenon in which the photoelectron is scattered back from the neighboring atoms: the back-scattered wave interferes with that of the primary photoelectron to produce a change in the absorption probability. The higher the x-ray energy  $E$  above the energy  $E_A$  of the absorption edge, the larger the wave vector  $k$  of the photoelectron and hence the scattering vector  $2k$  characterizing the diffraction process:

$$E - E_0 = \frac{\hbar^2 k^2}{2m_e}. \quad (1.50)$$

The spectrum of absorption vs.  $2k$  then shows oscillations similar to that of  $S(Q)$  in diffraction experiments. This has the advantage that the structural information in the spectrum is element specific, i.e., it relates only to the environment of the absorbing atoms. A disadvantage is that in liquids and glasses it is difficult to get structural information beyond the nearest neighbors of the absorbing atoms. With the powerful x-ray synchrotron sources now available, it is often preferable to use the AXS technique referred to above. However, in that case there is a correlation between the energy of the absorption edge and the maximum magnitude of the scattering vector  $Q$ , which determines the spatial resolution of the measurement, so with light elements, for example, those lighter than germanium ( $E_K = 11.1$  keV,  $Q_{\max} = 11.25 \text{ \AA}^{-1}$ ), other methods must be used: EXAFS, neutron diffraction with isotopic substitution, if suitable isotopes are available, or a combination of two or three techniques. Other advantages of EXAFS are that it is possible to obtain information about three-body correlations<sup>65</sup> and, since the

measurements are relatively rapid, structural changes can be studied during rapid variation of temperature or pressure.

The EXAFS signal  $\chi(k)$  is defined as the normalized deviation of the absorption coefficient  $\mu(k)$  of the sample from its value for an isolated atom  $\mu_0(k)$ :

$$\chi(k) = \frac{\mu(k) - \mu_0(k)}{\mu_0(k)}. \quad (1.51)$$

From scattering theory,

$$\chi(k) = \frac{|a(k)|}{k} \int_0^{\infty} \frac{p(r)}{r^2} e^{-\frac{2r}{\lambda(k)}} \sin[2kr + \phi(k)] dr, \quad (1.52)$$

where  $|a(k)|$  and  $\phi(k)$  are the characteristic back-scattering amplitude and phase shift due to scattering from the neighboring atoms,  $\lambda(k)$  is the mean free path of the photoelectron and  $p(r)$  is the bond length probability density, proportional to  $g(r)$ . In the case of small disorder, a Gaussian probability density with variance  $\sigma$  is normally assumed, and Equation 1.52 becomes

$$\chi(k) = - \sum_n \frac{C_1^n(j)}{(r_{1j}^n)^2} |f_j(k)| \exp\left(-2(\sigma_{1j}^n)^2 k^2\right) \exp\left(-\frac{2r}{\lambda(k)}\right) \sin[2kr_{1j}^n + \phi_j(k)] dr, \quad (1.53)$$

where, in the notation introduced in Section 1.2.1, the absorbing atom is taken as type 1 and the  $n$ th coordination shell is occupied by atoms of type  $j$ . For disordered systems like liquids, glasses, and crystalline materials at high temperatures, the assumption of symmetric peaks in  $g(r)$  is no longer valid, since the backscattering atoms feel the anharmonicity of the pair potential, and more realistic model functions must be employed.<sup>66</sup>

## 1.5 Inelastic Scattering

The dynamics of a system can be measured in an inelastic scattering experiment. For the past 50 years, this has been principally the province of neutron scattering, taking advantage of the fact that neutron beam emerging from moderators at reactors or spallation sources have typical energies on the order of 0.025 eV, corresponding to a temperature of about 300 K and comparable with typical energies of collective excitations in solids and liquids.<sup>4,29</sup> With cooled moderators and developments in neutron spectroscopic techniques such as neutron spin-echo spectrometry,<sup>67</sup> the usable energy range has been pushed down to  $10^{-6}$  eV and below, which provides a powerful probe of

relaxation processes in complex materials. X-rays start with the disadvantage that the energies must be on the order of  $10^4$  eV to access the  $Q$  values  $\sim 10 \text{ \AA}^{-1}$  of interest for investigations of the structure and dynamics of materials, so that an energy resolution of  $\sim 10^{-7}$  is required to get useful information about collective excitations in solids and liquids. Remarkably, this has been achieved with sophisticated design of energy monochromators and analyzers at the third-generation neutron sources such as the European Synchrotron Radiation Facility (ESRF) in Grenoble, France, the Advanced Photon Source (APS) in Argonne, Illinois, and SPRing-8 in Hyogo Prefecture, Japan. High-resolution IXS techniques have the advantage of overcoming the kinematic limitations affecting many neutron scattering studies and make it possible to study collective excitations in liquids and glasses at low  $Q$ .<sup>68</sup> This follows from the requirement that the velocity of the probe in such measurements must be appreciably higher than that of the collective excitation under study.

In inelastic scattering experiments, the energy transfer  $E$ —or equivalently the excitation frequency  $\omega = E/\hbar$ —is measured in addition to the scattering vector  $\vec{Q}$ . In the neutron case this is given by

$$E = \frac{\hbar^2 k_i^2}{2m_n} - \frac{\hbar^2 k_f^2}{2m_n}, \quad (1.54)$$

and in the x-ray case by

$$E = \hbar c k_i - \hbar c k_f. \quad (1.55)$$

To accomplish this measurement with either probe, both the magnitude and direction of both  $\vec{k}_i$  and  $\vec{k}_f$  must be defined in the design of the scattering apparatus.

The intensity of this scattering process is reduced to a double differential cross section, which for neutron scattering is given by

$$\frac{d^2\sigma}{d\Omega dE} = \frac{k_1}{k_0} \left\{ \sum_{a=1}^n c_a \bar{b}_a^2 \left| S(Q, E) + \left[ \sum_{a=1}^n c_a \left( \bar{b}_a^2 - \bar{b}_a^2 \right) \right] S^{\text{inc}}(Q, E) \right| \right\} \quad (1.56)$$

where the  $S(Q, E)$  and  $S^{\text{inc}}(Q, E)$  are the *coherent* and *incoherent partial scattering functions* (sometimes called *dynamical structure factors*).<sup>4,29</sup> Their physical significance can be understood if we make Fourier transforms to  $(Q, t)$  space:

$$S(Q, E) = \frac{1}{2\pi\hbar} \int_{-\infty}^{\infty} I(Q, t) e^{-iEt/\hbar} dt, \quad (1.57)$$

$$S^{\text{inc}}(Q, E) = \frac{1}{2\pi\hbar} \int_{-\infty}^{\infty} I^s(Q, t) e^{-iEt/\hbar} dt,$$

where  $I(Q,t)$  and  $I^s(Q,t)$  are called, respectively, the *total* and *self intermediate scattering functions*. Their values at zero time, or alternatively the integrals of  $S(Q,E)$  and  $S^{\text{inc}}(Q,E)$  over the entire energy region, are

$$I(Q,t=0) = \int_{-\infty}^{\infty} S(Q,E) dE = S(Q),$$

$$I^s(Q,t=0) = \int_{-\infty}^{\infty} S^{\text{inc}}(Q,E) dE = 1.$$
(1.58)

Thus,  $I(Q,t)$  represents the time development of the instantaneous partial structure factor  $S(Q)$  introduced in Section 1.2. On the other hand,  $I^s(Q,t)$  is related to the distribution in space that a single particle of type  $a$  is likely to occupy after time  $t$ . The time dependent quantity thus contains useful information about the trajectories of individual particles, whereas its value at time zero is trivially equal to one: each particle has not had time to move.

For multicomponent systems,  $S(Q,E)$  and correspondingly  $I(Q,t)$  are weighted averages over the different pairs of atom types, as in the diffraction case, while  $S^{\text{inc}}(Q,E)$  and  $I^s(Q,t)$  are averages over the different individual atom types. Furthermore, in neutron scattering, the relative contributions of coherent and incoherent scattering will depend on the various elements and isotopes in the samples. Most natural elements, as well as  $^2\text{H}$  and  $^6\text{Li}$ , are mostly coherent scatterers, whereas naturally abundant hydrogen is mostly incoherent and natural lithium and silver, for example, are a mixture of both (see Table 1.1). These facts must be taken into consideration in the interpretation of the scattering data. In IXS,  $b_a$  in the above equations and those that follow is replaced by  $f_a(Q)$ , the atomic form factor for species  $a$ . In this case, every atom of a given element scatters identically so the incoherent term does not appear. (In the x-ray field the term *incoherent* is often used instead to denote the Compton scattering, in which an x-ray scatters inelastically from an individual electron, providing information about the momentum distribution of the electrons in the ground state.)

In the case of a solid sample it is convenient to distinguish four dynamical regimes of neutron scattering, illustrated schematically in Figure 1.20 for the case of a disordered system like a liquid or a glass. For convenience we frame the discussion in terms of the weighted average structure factor  $S(Q)$  introduced in Section 1.2 and the corresponding weighted average scattering function  $S(Q,E)$ . Figure 1.20a shows a typical structure factor  $S(Q)$  in which we pick out a particular value of  $Q$ , say  $Q_1$ , and discuss the time development  $I(Q_1,t)$  of the correlations contributing to  $S(Q_1)$ . Figure 1.20b shows various time regimes that may appear in  $I(Q_1,t)$ , and Figure 1.20c the corresponding features in  $S(Q_1,E)$  obtained by the Fourier transform, Equation 1.57.

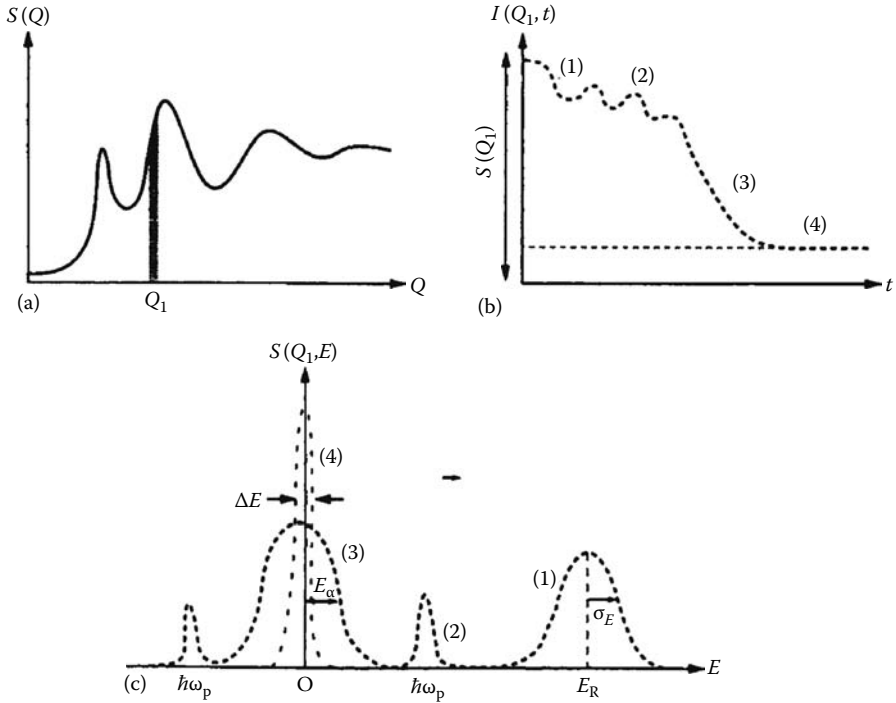


**FIGURE 1.20**

Schematic illustration of dynamical regimes probed by INS: (a) structure factor  $S(Q)$ , highlighting a specific scattering vector  $Q_i$ ; (b) intermediate-scattering function  $I(Q_i, t)$ ; and (c) scattering function  $S(Q_i, E)$ . The numbers denote the (1) recoil, (2) one-phonon, (3) quasielastic, and (4) elastic scattering regimes. (From Price, D.L., Saboungi, M.L., and Bermejo, F.J., Dynamical aspects of disorder in condensed matter, *Rep. Prog. Phys.*, 66, 413, 2003. With permission.)

1. The conceptually simplest scattering event is one that takes place as if the target nucleus is independent of its neighbors. This is in fact what happens at short times, where  $I(Q_i, t)$  falls off from its value at  $t=0$ , generally with an approximately Gaussian behavior. In the limit of large  $Q$ , this *recoil scattering* is the dominant contribution to  $S(Q_i, E)$ , consisting of a peak on the neutron energy-loss side ( $E > 0$ ) centered at the recoil energy  $E_R = \hbar^2 Q_i^2 / 2M$  with a shape that reflects the momentum distribution of the system in its ground state. In particular, the variance in energy is related to the mean kinetic energy  $K$ :  $\sigma_E^2 = K \hbar^2 Q_i^2 / M$ .
2. If there are collective excitations with a frequency  $\omega_p$ ,  $I(Q_i, t)$  has an oscillatory part and  $S(Q_i, E)$  has a peak centered at  $\pm \hbar \omega_p$ , generally referred to as *one-phonon scattering*. In single crystals the phonons can be labeled by a wave vector  $\vec{Q}$  and a branch index  $j$ : if the vibrational motion is harmonic,  $S(\vec{Q}_j, E)$  has a delta-function form  $S_j(\vec{Q}_j) \delta(E \pm \hbar \omega_p)$ . In a polycrystalline sample,  $S(Q_i, E)$  is an orientational

average over all directions of  $\vec{Q}$ . In glass, phonons still exist although they can no longer be labeled by a single value of  $Q$ .

3. If there are relaxation processes in which the correlations decay at some characteristic rate  $\alpha(Q)$  at a given value of  $Q$ ,  $S(Q_1, E)$  has a broadened component centered at  $E=0$ , called *quasielastic scattering*. Because of the higher energy resolution, quasielastic neutron scattering (QENS) is more commonly used. In the case of an exponential time decay  $\exp(-\alpha t)$ ,  $S(Q_1, E)$  has a Lorentzian form proportional to  $L_\alpha(Q, E)$ , where

$$L_\alpha(Q, E) = \frac{\hbar\alpha(Q)}{E^2 + [\hbar\alpha(Q)]^2}. \quad (1.59)$$

4. If there are structural correlations that last for long times (more precisely, times  $t \gg \hbar/\Delta E$  where  $\Delta E$  is the energy resolution of the experiment), which is the case in a solid where the atoms execute thermal motions about fixed equilibrium positions,  $I(Q_1, t)$  contains a non-zero time-independent term. This will give a delta-function  $S_{el}(Q_1) \delta(E)$  term in the scattering function, generally referred to as *elastic scattering*.

In a liquid, purely elastic scattering (regime 4) does not exist, and both the quasielastic scattering (regime 3) and collective excitations (regime 2) will generally be heavily damped and only show up as recognizable peaks at sufficiently low  $Q$ , sometimes called the *generalized hydrodynamic regime*. In the purely hydrodynamic regime that can be probed by light scattering, the collective excitations represent density fluctuations and are often referred to as Brillouin peaks, while the quasielastic scattering is due to entropy fluctuations and is called the Rayleigh peak. At higher  $Q$  the scattering reflects the dynamics of single particles, which evolves continuously into the recoil scattering at very high  $Q$  (regime 1).

As stated above, the integral of  $S(Q, E)$  over the entire range of  $E$  is equal to  $S(Q)$ . There is also a simple expression for the second energy moment of  $S(Q, E)$ :

$$\int_{-\infty}^{\infty} S(Q, E) E^2 dE = \frac{\hbar^2 Q^2}{2M} kT, \quad (1.60)$$

which, taken together with Equation 1.58, implies that the standard deviation of the width is given by

$$\sigma(E) = \sqrt{\frac{kT}{2MS(Q)}} \cdot \hbar Q. \quad (1.61)$$